



South Pacific carbon uptake controlled by West Antarctic Ice Sheet dynamics

Received: 8 May 2025

Accepted: 19 December 2025

Published online: 02 February 2026

Check for updates

Torben Struve¹✉, Frank Lamy¹, Frederik Gäng¹, Johann P. Klages¹,
Gerhard Kuhn¹, Oliver Esper², Lester Lembke-Jene¹ & Gisela Winckler^{1,3,4}

Increased supply of the micronutrient iron promotes export production in the iron-limited Southern Ocean, thus acting as a dynamic sink of atmospheric CO₂ that has amplified past climate variations. This mechanism is typically considered to be regulated by the amount and solubility of iron delivered by aeolian transport. Here we use sedimentological and geochemical tracers to investigate iron input and carbon uptake in the largest sector of the Southern Ocean Antarctic Zone. Our data show that millennial-scale variations in West Antarctic Ice Sheet dynamics controlled both the supply of particulate iron and lithogenic particle composition (affecting particle solubility) in the Pacific Antarctic Zone over the last 500,000 years. Rather than the total iron input, a higher abundance of chemically more pristine glaciomarine particles (high particle solubility) was critical for providing bioavailable iron, which enhanced export production. High lithogenic iron fluxes are characterized by chemically mature particles (low particle solubility), in particular during phases of pronounced ice loss in West Antarctica. The corresponding export production was low, indicating that this ‘ice-sheet–iron feedback’ is positive during these retreat phases. Accordingly, future West Antarctic Ice Sheet retreat is likely to decrease carbon uptake in the large Pacific sector of the Southern Ocean.

Southern Ocean Fe fertilization has attracted much attention due to its critical role in amplifying natural global cooling trends^{1–3} and as a strategy to artificially reduce atmospheric CO₂ levels^{1,4}. The current supply of Fe available for biological uptake from upwelling is insufficient for the Southern Ocean biological pump to operate at full capacity, thus leaving a large pool of unused macronutrients in the surface ocean^{5–7}. Accordingly, the additional (natural or anthropogenic) input of Fe induces phytoplankton blooms in this largest Fe-limited high-nutrient/low-chlorophyll area of the global ocean⁴.

Pleistocene glacial–interglacial cycles provide the opportunity to study the influence of changes in Fe input from continental sources on Southern Ocean primary production^{2,3,8–10}. The Subantarctic Zone (SAZ; Fig. 1) is typically considered the key region where natural

mineral-dust-driven Fe fertilization amplifies cooling trends during glacial periods^{2,3,9,10}. Increased input and partial dissolution of dust during glacials provided bioavailable Fe, thus promoting primary and export production in the SAZ that contributed to the accelerated reduction of atmospheric CO₂ levels^{2,3,9,11,12}. This is in contrast to the Antarctic Zone (AZ) south of the Antarctic Polar Front (APF) (Fig. 1). During glacial intervals, low primary production in the AZ results from the combined effects of reduced upwelling of macronutrients from the deep ocean^{13,14}, decreased sea surface temperatures¹⁵ and expanded sea-ice cover¹⁶. During interglacial intervals, the environmental conditions stimulate primary production^{13,14,17,18}. Carbon export to the deep ocean is high and efficient south of the APF under warm climate conditions^{19,20}, promoted by a higher abundance of ballast material

¹Institute for Chemistry and Biology of the Marine Environment (ICBM), Carl von Ossietzky Universität Oldenburg, Oldenburg, Germany. ²Department of Geosciences, Alfred Wegener Institute Helmholtz Centre for Polar and Marine Research, Bremerhaven, Germany. ³Columbia Climate School, Columbia University, New York, NY, USA. ⁴Lamont-Doherty Earth Observatory, Columbia University, Palisades, NY, USA. ✉e-mail: torben.struve@uni-oldenburg.de

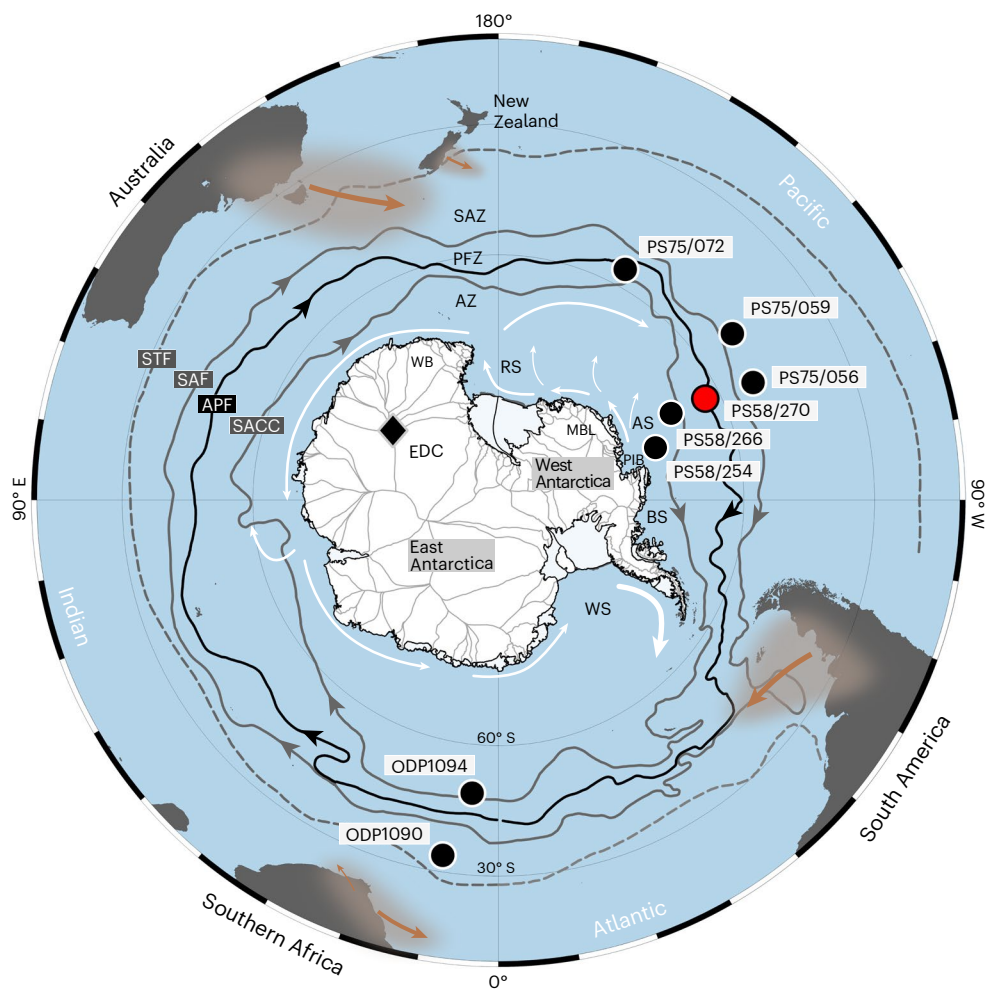


Fig. 1 | Map of the Southern Ocean. White arrows indicate iceberg drift^{38,39}. Brown plumes and arrows indicate major dust input trajectories^{29,68}. The key locations included in Figs. 2 and 3 are as follows: Antarctic ice core EPICA Dome C (EDC)^{37,65,66}, South Pacific sites PS58/254³², PS58/266, PS75/056, PS75/059^{9,29} and PS75/072¹⁴, and South Atlantic Ocean Drilling Program (ODP) Site 1090² and Site 1094¹³. Southern Ocean fronts are taken from ref. 69. STF, Subtropical Front;

SAF, Subantarctic Front; APF, Antarctic Polar Front; SACC, Southern Antarctic Circumpolar Current Front; SAZ, Subantarctic Zone; PFZ, Polar Frontal Zone; AZ, Antarctic Zone; RS, Ross Sea; WS, Weddell Sea; AS, Amundsen Sea; BS, Bellingshausen Sea; PIB, Pine Island Bay; MBL, Marie Byrd Land. Antarctic ice divides are shown as grey lines, and ice sheet and shelf boundary extensions as black lines^{70,71}. Base map produced with [Ocean Data View](#).

such as opal frustules produced by diatoms, resulting in a high potential of >50% for carbon export below the mixed layer²¹.

Chemically pristine (unweathered) sediments associated with glacial erosion and/or iceberg/sea-ice processes release more Fe, which is potentially available for uptake by primary producers in the Southern Ocean^{22–26}. A growing amount of observational data are improving our understanding of recent changes in Southern Ocean Fe cycling, primary production and carbon export²⁷, but the long-term variations over full glacial cycles are less well understood, and studies have focused on the dust-Fe feedback in the Southern Ocean SAZ^{2,3,9,10,28,29}.

Aside from dust-Fe input, the AZ generally receives considerable amounts of lithogenic and potentially bioavailable Fe from ice(berg) rafted detritus (IRD) (Fig. 1)^{22,24,25,30,31}. During glacials, lithogenic mass accumulation rates (MARs) increased near the ice-covered Antarctic continental shelves, whereas primary production was limited by increased sea-ice cover³². North of the zone of permanent sea-ice cover, growth potential was available for primary producers during the ice-free summer season in the AZ, even under peak glacial conditions^{16,18}. Notably, most existing reconstructions of mass accumulation in the AZ are based on sedimentation rates and limited by low temporal resolution³², and can easily be biased by post-depositional sediment reworking^{9,33}. This is a major issue in

quantitative reconstructions of marine particulate input and deposition (Methods), which implies that glacial–interglacial variations in lithogenic Fe fluxes, their geochemical composition and their influence on export production are overall relatively poorly constrained for the Southern Ocean AZ. Constant flux proxies such as the highly particle-reactive radioactive isotope 230-thorium (²³⁰Th) can help to overcome this problem and provide robust quantifications of marine particle fluxes for the past ~500 ka (kiloanni = 1,000 years)³³. Here, we combine ²³⁰Th-normalized tracers of lithic fluxes and export production with geochemical constraints on sediment mineralogy as indicators of Fe source and solubility in the surface ocean (Methods). Comparison with records from the SAZ further north shows that the mode of change in productivity and carbon uptake is controlled by bioavailable Fe from the partial dissolution of IRD in the South Pacific AZ, closely coupled to the dynamic interaction of the West Antarctic Ice Sheet (WAIS) with the underlying bedrock.

The source of iron

This work uses South Pacific sediment core PS58/270-5, recovered from a water depth of 4,981 m at 62.028° S and 116.123° W (Fig. 1). The lithology consists of diatom ooze that contains mud with some larger clasts (Methods and Extended Data Fig. 1) and the age model is

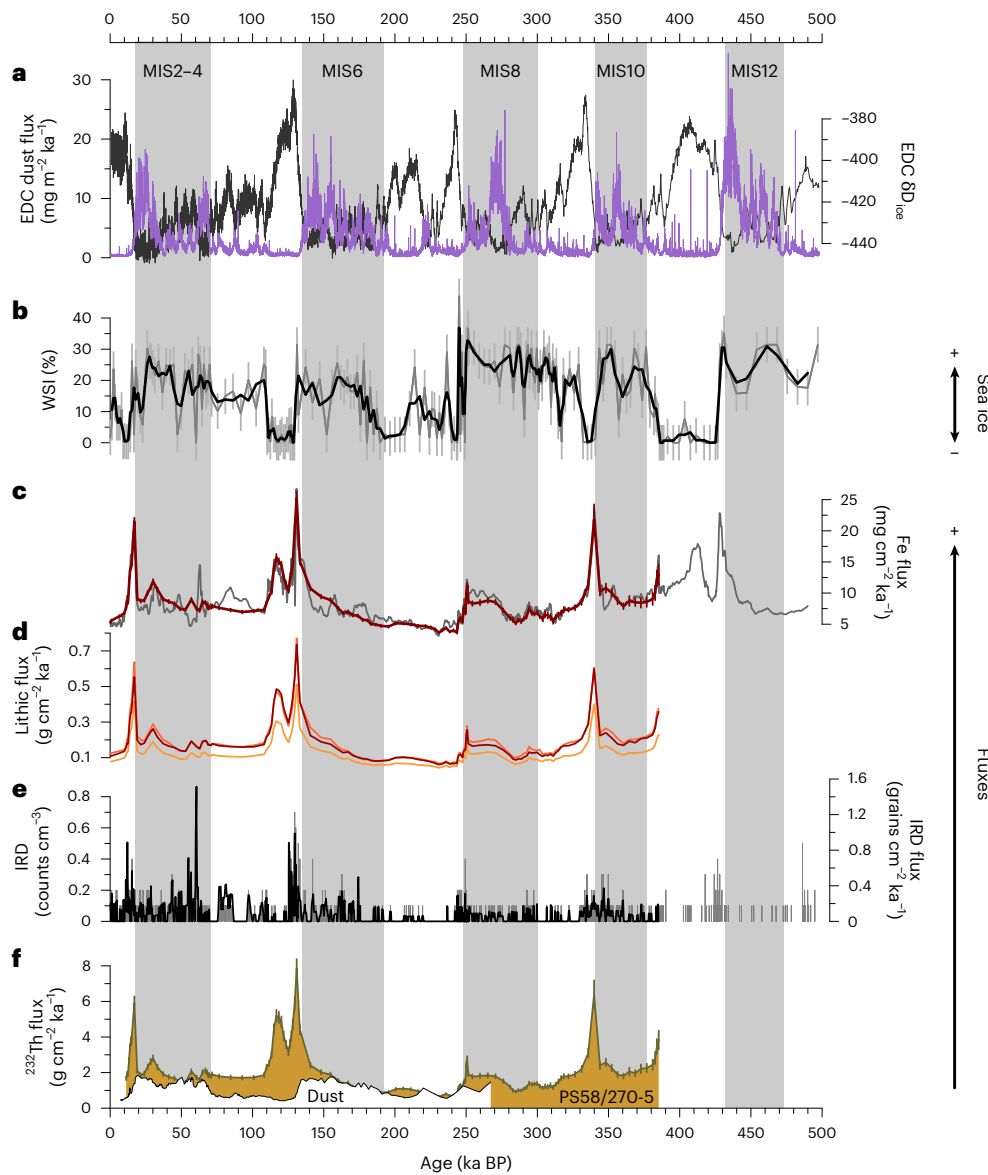


Fig. 2 | Timing, magnitude and composition of lithogenic input in the Southeast Pacific. **a**, EPICA Dome C ice core deuterium isotope (δD) (dark grey)⁶⁶ and dust flux (violet) records³⁷. **a**, time. **b**, Diatom-based reconstruction of winter sea ice (WSI) cover with three-point running average (black) and 5.5% uncertainty range (grey). **c**, Fe fluxes normalized to 230-thorium excess ($^{230}\text{Th}_{\text{xs}}$) for PS58/270-5 (dark red). Grey line: high-resolution Fe flux record calculated from interpolated mass fluxes and XRF scanner-derived calibrated Fe concentrations for the last ~386 ka. Fe fluxes before ~386 ka BP (BP = before present) were extrapolated based on the correlation of Fe fluxes and concentrations in the upper part (<386 ka BP) ($r = 0.75$, regression forced through 0). **d**, $^{230}\text{Th}_{\text{xs}}$ -normalized lithic fluxes, calculated using upper-

continental-crust compositions⁷² and Al (light orange), Ti (orange) and ^{232}Th (dark red) concentrations of PS58/270-5. **e**, Counts (grey) and fluxes (black) of >250- μm grains indicating IRD input at site PS58/270. **f**, Lithogenic ^{232}Th fluxes with propagated uncertainties for AZ core PS58/270-5 (olive lines with golden shading) compared to SAZ core PS75/056-1 (white shading) representing dust input for the last ~270 ka¹⁰. MIS, Marine Isotope Stage. Note that the grey bars are aligned with the end of peak glacial intervals, highlighting their offset to the maxima in lithic fluxes at site PS58/270. Error bars are shown as propagated errors where they exceed the line thickness, unless stated otherwise³⁴ (more details are provided in the Methods).

based primarily on diatom stratigraphy (Methods and Extended Data Figs. 2–4). Particle fluxes were calculated by normalization to ^{230}Th excess ($^{230}\text{Th}_{\text{xs}}$)^{33,34} (Methods and Extended Data Fig. 5). High-resolution element concentrations were calculated by combining discrete sample results with X-ray fluorescence scanner data (Extended Data Fig. 6). To trace the origin of the Fe in core PS58/270-5, we compared our Fe concentration data with refractory elements such as Al, Ti, Y and ^{232}Th (Fig. 2c–f and Extended Data Fig. 7). The excellent correlation between these lithogenic elements excludes relevant authigenic Fe enrichment³⁵ in our samples, thereby confirming the lithogenic origin of Fe at this location.

Mineral dust from arid and semi-arid areas in Australia/New Zealand and South America is typically considered the dominant supply of lithogenic particles in the remote South Pacific^{9,28,29,36}. However, the timing and magnitude of lithogenic fluxes in PS58/270-5 are clearly different to the nearly pure dust signals recorded in SAZ core PS75/056-1^{10,28} (Fig. 2f) and in Antarctic ice core samples³⁷ (Fig. 2a). Accordingly, when the lithogenic fluxes in PS58/270-5 exceed the fluxes in core PS75/056-1, non-aeolian transport must have contributed to the total lithogenic input at site PS58/270 (Fig. 2f). As the winter sea-ice cover is typically low and/or decreasing during the warming intervals of high lithogenic input (Fig. 2), sea-ice-hosted

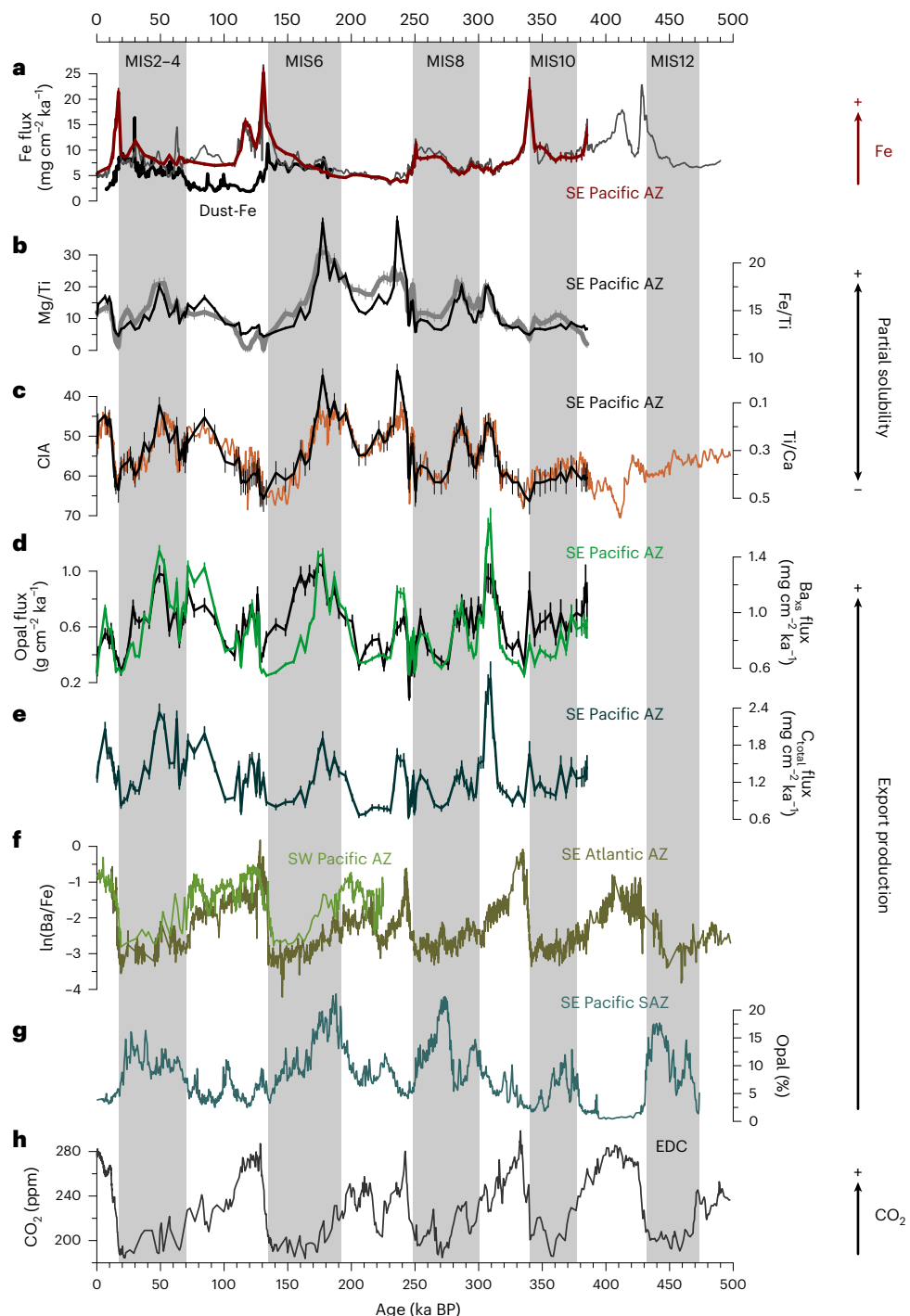


Fig. 3 | Mineral solubility and export production in the South Pacific.

a, Southeast Pacific Fe fluxes (red) for subantarctic core PS75/056-1 representing dust input¹⁰, and for core PS58/270-5. Grey line: high-resolution Fe flux record for PS58/270-5, calculated as described in the caption of Fig. 2. **b**, Mg-Ti (black) and Fe-Ti (grey) ratios of discrete sample digests. **c**, CIA (black) ($\text{CIA} = \text{Al}_2\text{O}_3 / [\text{Al}_2\text{O}_3 + \text{CaO}^* + \text{Na}_2\text{O}^* + \text{K}_2\text{O}] \times 100$, where CaO^* and Na_2O^* represent lithogenic CaO and Na_2O , respectively)⁴⁴, calculated from discrete sample measurements superimposed on calibrated XRF scanner based Ti-Ca concentration data for PS58/270-5 (red-brown) (also Extended Data Fig. 5c,e). Data shown in **b** and **c** reflect changes in lithogenic particle maturity indicative of partial solubility.

d, Opal (green) and Ba excess fluxes (black; Ba_{xs} : indicator for biogenic Ba deposition calculated as $\text{Ba}_{\text{xs}} = \text{Ba}_{\text{total}} - \text{Ba}_{\text{lithogenic}}$; $\text{Ba}_{\text{lithogenic}}$ calculated using thorium and titanium concentrations and upper continental crust values)⁷². **e**, Total carbon fluxes (C_{total}) as an indicator for organic carbon in core PS58/270-5. **f**, Ba/Fe as a qualitative indicator of export production in core PS75/072-4¹⁴ and at ODP Site 1094 in the Southeast Atlantic¹³. **g**, Opal content in core PS75/059-2, indicating export production in the subantarctic Southeast Pacific⁹. **h**, Antarctic ice core record of atmospheric CO_2 from EPICA Dome C⁶⁵. Specific locations are shown in Fig. 1. Error bars are shown as propagated errors where they exceed the line thickness³⁴. See Methods for more analytical details.

lithogenic particles are unlikely to cause the high total lithogenic fluxes at site PS58/270.

Instead, we consider IRD from Antarctica's ice shelves as an important source of lithogenic particles in the AZ. Consistent with icebergs

trajectories^{38–40}, Antarctic ice shelves are the only source that can support the high lithic Fe fluxes of up to $\sim 25 \text{ mg cm}^{-2} \text{ ka}^{-1}$, exceeding concurrent dust-Fe fluxes recorded in PS75/056-1^{10,28} by up to one order of magnitude (Figs. 2c,f and 3a) during phases of low sea-ice cover

(Fig. 2b). South Pacific time slice reconstructions of lithogenic fluxes near the APF show the highest fluxes in the Amundsen Sea sector^{18,41}. This west–east gradient suggests that East Antarctic sources play a minor role in Southeast Pacific sediment deposition, and further points to a West Antarctic origin of the lithogenic input recorded at site PS58/270 (Fig. 1). As a result, the lithogenic input at site PS58/270 reflects, overall, a mixed signal of dust input from lower latitude sources and IRD from West Antarctica, with the latter clearly dominating during deglacial and peak warming intervals (Fig. 2c,d).

Lithogenic input traces WAIS dynamics

The high contribution of ice-rafted sediments from West Antarctica to the total lithic input flux at the remote location of PS58/270-5 (up to ~90% during MIS5e) is corroborated by the corresponding increases in IRD fluxes (Fig. 2e). This is generally consistent with model results for sediment input from West Antarctica⁴², modern^{38,39} (Fig. 1) and past patterns of iceberg drift⁴⁰, as well as with reconstructions of Pleistocene changes in the erosional pattern of the marine-based parts of the East Antarctic ice sheet in the Wilkes subglacial basin⁴³.

The intervals of high IRD input comprise a large range of values from <45 to ~65 for the Chemical Index of Alteration (CIA = $\text{Al}_2\text{O}_3/[\text{Al}_2\text{O}_3 + \text{CaO}^* + \text{Na}_2\text{O}^* + \text{K}_2\text{O}] \times 100$)⁴⁴ (Fig. 3c). Higher values reflect increased loss of the more soluble elements Ca, Na and K relative to the refractory Al, thus tracing exposure to chemical weathering and/or provenance⁴⁴ (Methods). Physical grinding of rocks and sediments is enhanced by glacial activity, so we ascribe the low CIA and Ti/Ca values to the supply of largely unweathered (fresh) high-Fe/Mg rock debris and minerals from West Antarctic sources, such as the hornblende and biotite-rich rock formations in Marie Byrd Land⁴⁵ (Fig. 1). This is supported by other element ratios sensitive to changes in sediment mineralogy. For example, high Fe/Ti, Fe/Th, Mg/Ti and Mg/Th (relatively enriched Fe and Mg) correspond systematically with low CIA and Ti/Ca (Fig. 3b,c and Extended Data Figs. 8a–d, 9 and 10).

The extremely dry and cold conditions in Antarctica generally preclude high chemical weathering rates, and the chemical leaching of freshly ground rock material during (sub)glacial melt processes^{46,47} seems unlikely to drive the large CIA variations in PS58/270-5. However, sediments with elevated CIA values of ~70 and high Ti/Ca of ~1 are common on the West Antarctic shelves^{48–50}. Their erosion could explain the increased CIA and Ti/Ca in PS58/270-5 during peak glacial intervals with maxima in WAIS extent and subsequent deglacial ice sheet decay⁵¹. Importantly, lithologies with high CIA and Ti/Ca are not limited to the West Antarctic shelf areas, but are derived from physical erosion of chemically weathered pre-Oligocene West Antarctic sediment rocks, which contain high amounts of kaolinite (~20%)^{32,49,50}.

Rock debris at the base of Byrd ice core in West Antarctica containing up to ~40% kaolinite⁵² suggests that this area could be an ‘upstream’ source of the kaolinite-rich shelf deposits transported toward Pine Island Bay (Amundsen Sea)⁵⁰, the Antarctic continental margin at site PS58/254³² (Extended Data Fig. 9b), open AZ site PS58/266-3 (Fig. 1 and Supplementary Fig. 1) and/or the Ross Sea shelf⁵². Erosion of these lithologies in central West Antarctica may therefore explain high CIA and high Ti/Ca values corresponding typically with high IRD and total lithogenic fluxes during peak warm intervals ($r = 0.67, P < 0.001, n = 139$ for CIA and Fe fluxes) at site PS58/270 (Fig. 3a,c). This is particularly interesting during MIS5e and 11, when high lithic input fluxes and high

CIA values (Fig. 3a,c) coincide with large-scale retreat of the dynamic, marine-based ice sheets in East and West Antarctica^{43,53–55}.

The close relationship between sediment origin and lithogenic fluxes suggests further that the lithogenic input is driven primarily by ice dynamics at the source rather than by oceanographic and atmospheric conditions during transport. Therefore, the observed changes in lithogenic flux of up to an approximately fivefold increase relative to the Late Holocene levels (Fig. 2c,d,f) are ascribed to WAIS dynamics driving variations in iceberg size, abundance and/or sediment load when travelling towards the open South Pacific (Fig. 4). The timing and magnitude of WAIS-driven lithogenic input fluxes for PS58/270-5 are generally consistent with Last Glacial Maximum–Holocene time slice data from the South Pacific¹⁸, but clearly offset from typical glacial–interglacial variations in the dust-dominated Pacific SAZ^{2,26,28} and from other sectors of the Southern Ocean AZ where different ice-sheet and IRD dynamics led to high lithogenic fluxes during glacial intervals^{56,57}. Importantly, these processes supply essential micronutrients including Fe to the Fe-depleted Southern Ocean^{24,30}, implying that WAIS dynamics have a far-reaching impact on marine primary production in the large Pacific AZ.

Export production driven by particle solubility

The peaks in export production do not align with interglacial intervals of high upwelling intensity typically considered to enhance nutrient supply (including Fe)⁵⁸ and primary production in other sectors of the Southern Ocean AZ^{13,14,59} (Fig. 3d–f), nor with the timing of changes in the SAZ (Fig. 3g). Instead, elevated export production corresponds systematically with the input of fresh, unweathered material, indicated by low CIA values, which are associated with a higher abundance of more soluble Fe(II)/Mg-rich (mafic) rocks and rock minerals such as hornblende and biotite (Extended Data Figs. 8a–g, 9d,e and 10)²⁶. This is expressed in a negative correlation between opal fluxes and the CIA ($r = -0.69, P < 0.0001, n = 139$) as well as with Ti/Ca ($r = -0.65, P < 0.0001, n = 139$) over the past 400 ka (Fig. 3c,d and Extended Data Fig. 8f,g).

A striking example of this relationship is again MIS5e, when total Fe fluxes peaked (Fig. 3a) and opal, carbon and Ba_{xs} fluxes indicate low export production (Fig. 3d,e), despite largely ice-free conditions (Fig. 2b) and strong upwelling leading to high macronutrient availability in the Southern Ocean AZ^{13,14,59}. Only with decreasing CIA and Ti/Ca (more fresh material) is a pronounced increase in export production evident, starting at ~90 ka BP (kiloanni before present) (Fig. 3b–e). In contrast, peak glacial intervals feature reduced export production, high CIA and high Ti/Ca values (weathered material), probably due to the maxima in WAIS extent⁵¹ delivering primarily West Antarctic shelf sediments^{48,50} to site PS58/270. Increased sea-ice cover (that is, a shorter growth season) and/or reduced availability of macronutrients¹⁴ may have further contributed to the minima in export production at these times (Figs. 3d–f and 4).

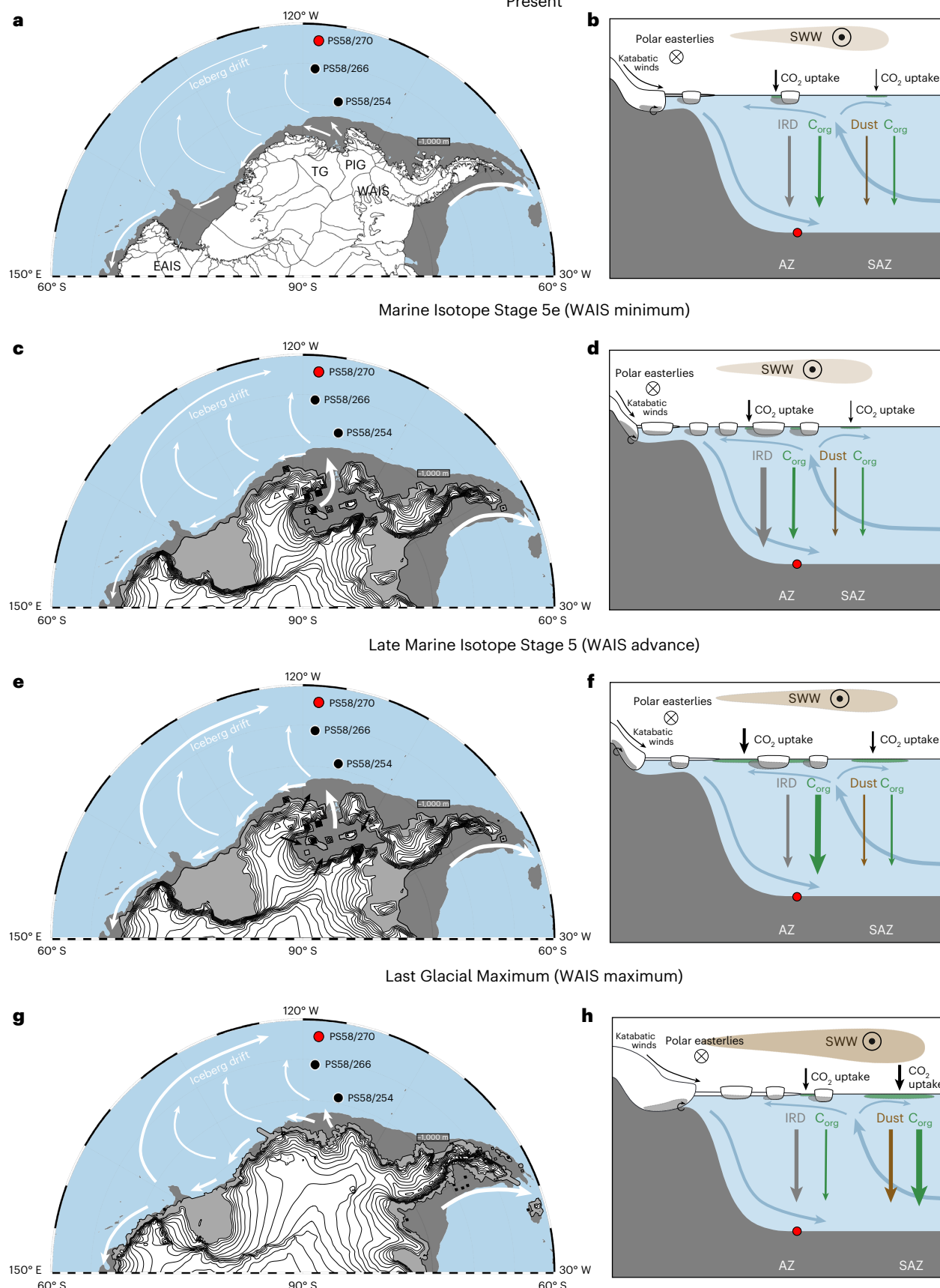
Based on these observations, we propose that the chemical composition/maturity of the lithogenic sediments traces particle solubility and Fe bioavailability acting to control export production in the Pacific AZ. Modern observations show that the chemical form and bioavailability of Fe, rather than the total flux, are important factors controlling primary productivity⁶⁰. Icebergs carry large amounts of particulate Fe that partially dissolves in melt- and seawater, thus increasing the concentration of bioavailable Fe and productivity upon

Fig. 4 | Schematic of major phases of ice-driven carbon uptake in the Southeast Pacific over the last glacial cycle. a,c,e,g. Overview maps of modern^{70,71} and modelled past Antarctic ice-sheet extent^{53,54} for present (a), marine isotope stage (MIS) 5e (c), late MIS5 (e) and the Last Glacial Maximum (g). Iceberg drift paths are indicated by white arrows^{38–40}. Ice shelves in the model results are indicated in light grey. Note that different parameterization of this ice-sheet model can produce a much stronger retreat of grounded ice in the Ross Ice Shelf region for MIS5e⁵⁵. **b,d,f,h.** Simplified transects summarizing location,

magnitude and impact of IRD in the South Pacific AZ for the respective time intervals, in comparison with concurrent dust-dominated Fe fertilization in the SAZ. Red filled circles show the location of site PS58/270. Dust plumes are indicated in brown. Blue arrows indicate Southern Ocean upwelling and water mass transformation. WAIS, West Antarctic Ice Sheet; PIG, Pine Island Glacier; TG, Thwaites Glacier; SWW, Southern Westerly Winds; C_{org}, organic carbon. Base maps were produced with [Ocean Data View](#).

melting and fragmentation of icebergs over large ocean areas^{22,24,25,38,39}. We note that our dataset is unable to constrain the biogeochemical cycling of the Fe fraction released from lithogenic particles in the surface ocean (including Fe recycling, precipitation, scavenging or

dilution during transport). However, the significant correlations of our export production proxies with our sedimentary mineralogy indicators (Extended Data Fig. 8) strongly suggest a causal link between those otherwise independent parameters. This is consistent with



laboratory experiments showing that unweathered mafic Fe(II)-rich sediments release more bioavailable Fe into seawater than weathered sediments²⁶, a mechanism that has promoted diatom growth in the Southern Ocean SAZ during the last glacial cycle¹⁰. A similar impact on export production has recently been linked to short-lived IRD input in the Atlantic SAZ⁶¹. Available evidence reflects the critical influence of provenance/mineralogy of subglacially eroded Antarctic bedrock on the supply of bioavailable Fe to the large South Pacific AZ over the last ~500 ka (Figs. 1 and 4).

Interestingly, the extended minima in export production during MIS2–4 and MIS6 in Southwest Pacific AZ core PS75/072-4¹⁴ (Fig. 3f) are not evident in the Southeast Pacific AZ (Fig. 3d,e), despite their similar distance from the APF (Fig. 1). The difference in timing of export production between the Southwest and Southeast Pacific implies that the lithogenic Fe input from West Antarctica was not a critical influence on export production in the Southwest Pacific. This can be related either to a more direct control via macronutrient availability in the Southwest Pacific¹⁴, and/or the lithogenic material reaching the Southwest Pacific was delivered from different sources with reduced variation in bioavailable Fe supply. The latter would imply that the West Antarctic-derived sediments reaching site PS58/270 did not pass through the western Ross Gyre transporting lithogenic material to the Southwest Pacific⁴⁰. Instead, the IRD was delivered directly from West Antarctica towards the open Southeast Pacific following modern iceberg drift patterns (Figs. 1 and 4) and in agreement with data-model integration of sediment provenance⁴² and lithogenic particle flux data^{18,41}.

Impact of WAIS-driven Fe fertilization on carbon uptake

The peak opal fluxes of $-1.2 \text{ g cm}^{-2} \text{ ka}^{-1}$ recorded in PS58/270-5 are higher than the maxima of most opal flux reconstructions from the Pacific^{9,17,18}, Indian⁵⁷ and Atlantic SAZ^{56,62} (typically $<0.5 \text{ g cm}^{-2} \text{ ka}^{-1}$) that are considered to play a major role in the drawdown of atmospheric CO₂ during glacial intervals²⁹. To showcase the relevance of the observed variations in opal, carbon and Ba_{xs} fluxes (Fig. 3d,e) for glacial–interglacial CO₂ levels, we carried out a simple calculation based on the assumption that the relative variations in export production at the remote site PS58/270 (Fig. 1) are diagnostic for the entire Southeast Pacific AZ (area south of $\sim 60^\circ \text{S}$, between $\sim 60^\circ \text{W}$ and $\sim 140^\circ \text{W}$, excluding shelf areas). That is, icebergs would continuously release bioavailable Fe to the AZ during their journey from the West Antarctic margin towards site PS58/270^{22,42}. Observational data from this region show an average annual particulate organic carbon (POC) flux of 42.5 g C m^{-2} out of the mixed layer for the years 2016/2017 and 2017/2018⁶³. Assuming that this flux represents Late Holocene levels, the two- to threefold increase in peak Ba_{xs}, carbon and opal fluxes in comparison with Late Holocene values suggests an increase of carbon export in the Southeast Pacific from $-0.18 \text{ Pg C a}^{-1}$ to $-0.36\text{--}0.54 \text{ Pg C a}^{-1}$. This is equivalent to an increased reduction in atmospheric CO₂ from -0.08 to $-0.17\text{--}0.25 \text{ ppm a}^{-1}$.

These estimates do not consider possible changes in ocean stratification⁷, nutrient and carbon cycling⁶, areas outside the Pacific AZ with occasional increases in IRD-driven export production⁶¹ or ecological community shifts^{8,64} that may act to further alter the net effect on atmospheric CO₂ concentrations. However, these calculations show that the magnitude of WAIS-driven changes in export production in the Southeast Pacific AZ could have a notable influence on atmospheric CO₂ levels on multidecadal to orbital time-scales. Because this mechanism is dependent on the character of the eroded Antarctic bedrock, the timing is complex and differs from insolation-driven glacial–interglacial climate variations. The increased export production, and thus an enhanced CO₂ removal potential, is typically observed during interglacial and early glacial cooling intervals^{65,66} (Figs. 2a and 3d,e). Consequently, these processes in the Southeast Pacific AZ would have contributed to the $\sim 50\text{--}60 \text{ ppm}$ decreases in atmospheric CO₂ observed early in

the Pleistocene glacial cycles⁶⁵ that are unrelated to the Southern Ocean dust-Fe feedback^{2,3,9,10} (Fig. 3a,h and Extended Data Fig. 9g). As such, the WAIS-driven increases in export production and carbon sequestration in the Pacific AZ amplified early glacial cooling when the Southern Ocean dust-Fe feedback was weak.

Moreover, the preserved Late Holocene sedimentary carbon fluxes of $\sim 1.3 \text{ mg cm}^{-2} \text{ ka}^{-1}$ at site PS58/270 (Fig. 3e) are only $\sim 0.03\%$ of the observed export fluxes from the mixed layer⁶³. Assuming that this proportion was invariable over Pleistocene glacial–interglacial cycles, the intervals of elevated productivity resulted in an increase in long-term sedimentary carbon storage in the Southeast Pacific AZ that was equivalent to $\sim 0.5 \text{ ppm}$ of atmospheric CO₂ per 10 ka. The accumulative effect of the repeated increases in WAIS-controlled sedimentary carbon deposition would therefore have contributed to the long-term Pliocene–Pleistocene cooling trend.

These findings from the South Pacific highlight the need for similar studies from other sectors of the Southern Ocean to better constrain the sensitivity of the Southern Ocean CO₂ sink and biogeochemical cycles to changes in subglacial erosion on different time-scales. We expect that future warming and ice loss in Antarctica will induce additional complexity to the predicted changes in Southern Ocean primary production, biogeochemical cycles, ecosystems and ultimately the carbon budget^{5,15,67} through a positive ‘ice-sheet–Fe feedback’ when the retreating WAIS erodes highly weathered subglacial lithologies, providing reduced amounts of bioavailable Fe to the South Pacific AZ.

Online content

Any methods, additional references, Nature Portfolio reporting summaries, source data, extended data, supplementary information, acknowledgements, peer review information; details of author contributions and competing interests; and statements of data and code availability are available at <https://doi.org/10.1038/s41561-025-01911-0>.

References

1. Martin, J. H. Glacial–interglacial CO₂ change: the iron hypothesis. *Paleoceanogr. Paleoclimatol.* **5**, 1–13 (1990).
2. Martínez-García, A. et al. Southern Ocean dust–climate coupling over the past four million years. *Nature* **476**, 312–315 (2011).
3. Martínez-García, A. et al. Iron fertilization of the Subantarctic Ocean during the last Ice Age. *Science* **343**, 1347–1350 (2014).
4. Boyd, P. W. et al. Mesoscale iron enrichment experiments 1993–2005: synthesis and future directions. *Science* **315**, 612–617 (2007).
5. Ryan-Keogh, T. J., Thomalla, S. J., Monteiro, P. M. S. & Tagliabue, A. Multidecadal trend of increasing iron stress in Southern Ocean phytoplankton. *Science* **379**, 834–840 (2023).
6. Sarmiento, J. L., Gruber, N., Brzezinski, M. A. & Dunne, J. P. High-latitude controls of thermocline nutrients and low latitude biological productivity. *Nature* **427**, 56–60 (2004).
7. Sigman, D. M. & Boyle, E. A. Glacial/interglacial variations in atmospheric carbon dioxide. *Nature* **407**, 859–869 (2000).
8. Abelmann, A., Gersonde, R., Cortese, G., Kuhn, G. & Smetacek, V. Extensive phytoplankton blooms in the Atlantic sector of the glacial Southern Ocean. *Paleoceanogr. Paleoclimatol.* **21**, PA1013 (2006).
9. Lamy, F. et al. Increased dust deposition in the Pacific Southern Ocean during glacial periods. *Science* **343**, 403–407 (2014).
10. Shoenfelt, E. M., Winckler, G., Lamy, F., Anderson, R. F. & Bostick, B. C. Highly bioavailable dust-borne iron delivered to the Southern Ocean during glacial periods. *Proc. Natl. Acad. Sci. USA* **115**, 11180–11185 (2018).
11. Khatiwala, S., Schmittner, A. & Muglia, J. Air-sea disequilibrium enhances ocean carbon storage during glacial periods. *Sci. Adv.* **5**, eaaw4981 (2019).

12. Shaffer, G. & Lambert, F. In and out of glacial extremes by way of dust-climate feedbacks. *Proc. Natl Acad. Sci. USA* **115**, 2026–2031 (2018).

13. Jaccard, S. L. et al. Two modes of change in Southern Ocean productivity over the past million years. *Science* **339**, 1419–1423 (2013).

14. Studer, A. S. et al. Antarctic Zone nutrient conditions during the last two glacial cycles. *Paleoceanogr. Paleoclimatol.* **30**, 845–862 (2015).

15. Hutchins, D. A. & Boyd, P. W. Marine phytoplankton and the changing ocean iron cycle. *Nat. Clim. Change* **6**, 1072–1079 (2016).

16. Benz, V., Esper, O., Gersonde, R., Lamy, F. & Tiedemann, R. Last Glacial Maximum sea surface temperature and sea-ice extent in the Pacific sector of the Southern Ocean. *Quat. Sci. Rev.* **146**, 216–237 (2016).

17. Chase, Z., Anderson, R. F., Fleisher, M. Q. & Kubik, P. W. Scavenging of ^{230}Th , ^{231}Pa and ^{10}Be in the Southern Ocean (SW Pacific sector): the importance of particle flux, particle composition and advection. *Deep Sea Res. Part II Top. Stud. Oceanogr.* **50**, 739–768 (2003).

18. Bradtmiller, L. I., Anderson, R. F., Fleisher, M. Q. & Burckle, L. H. Comparing glacial and Holocene opal fluxes in the Pacific sector of the Southern Ocean. *Paleoceanogr. Paleoclimatol.* **24**, PA2214 (2009).

19. Arteaga, L. A., Pahlow, M., Bushinsky, S. M. & Sarmiento, J. L. Nutrient controls on export production in the Southern Ocean. *Glob. Biogeochem. Cycles* **33**, 942–956 (2019).

20. Weber, T., Cram, J. A., Leung, S. W., DeVries, T. & Deutsch, C. Deep ocean nutrients imply large latitudinal variation in particle transfer efficiency. *Proc. Natl Acad. Sci. USA* **113**, 8606–8611 (2016).

21. Stirnemann, L. et al. A circum-Antarctic plankton isoscape: carbon export potential across the summertime Southern Ocean. *Glob. Biogeochem. Cycles* **38**, e2023GB007808 (2024).

22. Duprat, L. P. A. M., Bigg, G. R. & Wilton, D. J. Enhanced Southern Ocean marine productivity due to fertilization by giant icebergs. *Nat. Geosci.* **9**, 219–221 (2016).

23. Lannuzel, D. et al. Distribution of dissolved iron in Antarctic sea ice: Spatial, seasonal, and inter-annual variability. *J. Geophys. Res.* <https://doi.org/10.1029/2009jg001031> (2010).

24. Raiswell, R. et al. Potentially bioavailable iron delivery by iceberg-hosted sediments and atmospheric dust to the polar oceans. *Biogeosciences* **13**, 3887–3900 (2016).

25. Raiswell, R., Benning, L. G., Tranter, M. & Tulaczyk, S. Bioavailable iron in the Southern Ocean: the significance of the iceberg conveyor belt. *Geochem. Trans.* **9**, 7 (2008).

26. Shoenfelt, E. M. et al. High particulate iron(II) content in glacially sourced dusts enhances productivity of a model diatom. *Sci. Adv.* **3**, e1700314 (2017).

27. Boyd, P. W. et al. The role of biota in the Southern Ocean carbon cycle. *Nat. Rev. Earth Environ.* **5**, 390–408 (2024).

28. van der Does, M. et al. Opposite dust grain-size patterns in the Pacific and Atlantic sectors of the Southern Ocean during the last 260,000 years. *Quat. Sci. Rev.* **263**, 106978 (2021).

29. Struve, T. et al. Systematic changes in circumpolar dust transport to the Subantarctic Pacific Ocean over the last two glacial cycles. *Proc. Natl Acad. Sci. USA* **119**, e2206085119 (2022).

30. Laufkötter, C., Stern, A. A., John, J. G., Stock, C. A. & Dunne, J. P. Glacial iron sources stimulate the Southern Ocean carbon cycle. *Geophys. Res. Lett.* **45**, 13,377–13,385 (2018).

31. van der Does, M. et al. Late Holocene dust deposition fluxes over the entire South Atlantic Ocean. *Geochem. Geophys. Geosyst.* **25**, e2023GC01105 (2024).

32. Hillenbrand, C.-D., Kuhn, G. & Frederichs, T. Record of a Mid-Pleistocene depositional anomaly in West Antarctic continental margin sediments: an indicator for ice-sheet collapse?. *Quat. Sci. Rev.* **28**, 1147–1159 (2009).

33. Costa, K. M. et al. ^{230}Th normalization: new insights on an essential tool for quantifying sedimentary fluxes in the modern and quaternary ocean. *Paleoceanogr. Paleoclimatol.* **35**, e2019PA003820 (2020).

34. Struve, T. et al. Sediment composition and particle flux reconstructions for the Southeast Pacific Antarctic Zone. *PANGEA* <https://doi.org/10.1594/PANGAEA.982690> (2025).

35. Winckler, G., Anderson, R. F., Jaccard, S. L. & Marcantonio, F. Ocean dynamics, not dust, have controlled equatorial Pacific productivity over the past 500,000 years. *Proc. Natl Acad. Sci. USA* **113**, 6119–6124 (2016).

36. Struve, T. et al. A circumpolar dust conveyor in the glacial Southern Ocean. *Nat. Commun.* **11**, 5655 (2020).

37. Lambert, F., Bigler, M., Steffensen, J. P., Hutterli, M. & Fischer, H. Centennial mineral dust variability in high-resolution ice core data from Dome C, Antarctica. *Clim. Past* **8**, 609–623 (2012).

38. Tournadre, J., Bouhier, N., Girard-Ardhuin, F. & Rémy, F. Antarctic icebergs distributions 1992–2014. *J. Geophys. Res. Oceans* **121**, 327–349 (2016).

39. Rackow, T. et al. A simulation of small to giant Antarctic iceberg evolution: differential impact on climatology estimates. *J. Geophys. Res. Oceans* **122**, 3170–3190 (2017).

40. Hemming, S. R. et al. Strontium isotope tracing of terrigenous sediment dispersal in the Antarctic Circumpolar Current: implications for constraining frontal positions. *Geochem. Geophys. Geosyst.* **8**, Q06N13 (2007).

41. Wengler, M. et al. A geochemical approach to reconstruct modern dust fluxes and sources to the South Pacific. *Geochim. Cosmochim. Acta* **264**, 205–223 (2019).

42. Marschalek, J. W. et al. Quantitative sub-ice and marine tracing of Antarctic sediment provenance (TASP v1.0). *Geosci. Model Dev.* **18**, 1673–1708 (2025).

43. Wilson, D. J. et al. Ice loss from the East Antarctic Ice Sheet during late Pleistocene interglacials. *Nature* **561**, 383–386 (2018).

44. Nesbitt, H. W. & Young, G. M. Early Proterozoic climates and plate motions inferred from major element chemistry of lutites. *Nature* **299**, 715–717 (1982).

45. Pankhurst, R. J., Weaver, S. D., Bradshaw, J. D., Storey, B. C. & Ireland, T. R. Geochronology and geochemistry of pre-Jurassic superterranes in Marie Byrd Land, Antarctica. *J. Geophys. Res. Solid Earth* **103**, 2529–2547 (1998).

46. Marra, K. R., Elwood Madden, M. E., Soreghan, G. S. & Hall, B. L. Chemical weathering trends in fine-grained ephemeral stream sediments of the McMurdo Dry Valleys, Antarctica. *Geomorphology* **281**, 13–30 (2017).

47. Wadham, J. L. et al. Biogeochemical weathering under ice: size matters. *Global Biogeochem. Cycles* <https://doi.org/10.1029/2009gb003688> (2010).

48. Lang Farmer, G., Licht, K., Swope, R. J. & Andrews, J. Isotopic constraints on the provenance of fine-grained sediment in LGM tills from the Ross Embayment, Antarctica. *Earth Planet. Sci. Lett.* **249**, 90–107 (2006).

49. Simões Pereira, P. et al. Geochemical fingerprints of glacially eroded bedrock from West Antarctica: detrital thermochronology, radiogenic isotope systematics and trace element geochemistry in Late Holocene glacial-marine sediments. *Earth Sci. Rev.* **182**, 204–232 (2018).

50. Simões Pereira, P. et al. The geochemical and mineralogical fingerprint of West Antarctica's weak underbelly: Pine Island and Thwaites glaciers. *Chem. Geol.* **550**, 119649 (2020).

51. Bentley, M. J. et al. A community-based geological reconstruction of Antarctic Ice Sheet deglaciation since the Last Glacial Maximum. *Quat. Sci. Rev.* **100**, 1–9 (2014).

52. Marschalek, J. W. et al. Byrd ice core debris constrains the sediment provenance signature of Central West Antarctica. *Geophys. Res. Lett.* **51**, e2023GL106958 (2024).

53. Clark, P. U. et al. Oceanic forcing of penultimate deglacial and last interglacial sea-level rise. *Nature* **577**, 660–664 (2020).

54. Golledge, N. R. et al. Retreat of the Antarctic ice sheet during the last interglaciation and implications for future change. *Geophys. Res. Lett.* **48**, e2021GL094513 (2021).

55. Wolff, E. W. et al. The Ronne Ice Shelf survived the last interglacial. *Nature* **638**, 133–137 (2025).

56. Frank, M. et al. Similar glacial and interglacial export bioproductivity in the Atlantic Sector of the Southern Ocean: multiproxy evidence and implications for glacial atmospheric CO₂. *Paleoceanogr. Paleoclimatol.* **15**, 642–658 (2000).

57. Thöle, L. M. et al. Glacial-interglacial dust and export production records from the Southern Indian Ocean. *Earth Planet. Sci. Lett.* **525**, 115716 (2019).

58. Tagliabue, A. et al. Hydrothermal contribution to the oceanic dissolved iron inventory. *Nat. Geosci.* **3**, 252–256 (2010).

59. Ai, X. E. et al. Southern Ocean upwelling, Earth's obliquity, and glacial-interglacial atmospheric CO₂ change. *Science* **370**, 1348–1352 (2020).

60. Fourquez, M. et al. Chasing iron bioavailability in the Southern Ocean: insights from *Phaeocystis antarctica* and iron speciation. *Sci. Adv.* **9**, eadf9696 (2023).

61. Barkley, A. E. et al. Patagonian dust, Agulhas Current, and Antarctic ice-rafted debris contributions to the South Atlantic Ocean over the past 150,000 years. *Proc. Natl Acad. Sci. USA* **121**, e2402120121 (2024).

62. Anderson, R. F. et al. Biological response to millennial variability of dust and nutrient supply in the Subantarctic South Atlantic Ocean. *Philos. Trans. R. Soc. Math. Phys. Eng. Sci.* **372**, 20130054 (2014).

63. Lacour, L., Llort, J., Briggs, N., Strutton, P. G. & Boyd, P. W. Seasonality of downward carbon export in the Pacific Southern Ocean revealed by multi-year robotic observations. *Nat. Commun.* **14**, 1278 (2023).

64. Moore, J. K., Abbott, M. R., Richman, J. G. & Nelson, D. M. The southern ocean at the Last Glacial Maximum: a strong sink for atmospheric carbon dioxide. *Glob. Biogeochem. Cycles* **14**, 455–475 (2000).

65. Lüthi, D. et al. High-resolution carbon dioxide concentration record 650,000–800,000 years before present. *Nature* **453**, 379–382 (2008).

66. Jouzel, J. et al. Orbital and millennial Antarctic climate variability over the past 800,000 years. *Science* **317**, 793–796 (2007).

67. Henley, S. F. et al. Changing biogeochemistry of the Southern Ocean and its ecosystem implications. *Front. Mar. Sci.* <https://doi.org/10.3389/fmars.2020.00581> (2020).

68. Neff, P. D. & Bertler, N. A. N. Trajectory modeling of modern dust transport to the Southern Ocean and Antarctica. *J. Geophys. Res. Atmos.* **120**, 2015JD023304 (2015).

69. Orsi, A. H., Whitworth, T. III & Nowlin, W. D. Jr. On the meridional extent and fronts of the Antarctic circumpolar current. *Deep Sea Res. Part Oceanogr. Res. Pap.* **42**, 641–673 (1995).

70. Rignot, E., Jacobs, S., Mouginot, J. & Scheuchl, B. Ice-shelf melting around Antarctica. *Science* **341**, 266–270 (2013).

71. Mouginot, J., Rignot, E., Scheuchl, B. & Millan, R. Comprehensive annual ice sheet velocity mapping using Landsat-8, Sentinel-1, and RADARSAT-2 data. *Remote Sens.* **9**, 364 (2017).

72. Taylor, S. R. & McLennan, S. M. The geochemical evolution of the continental crust. *Rev. Geophys.* **33**, 241–265 (1995).

Publisher's note Springer Nature remains neutral with regard to jurisdictional claims in published maps and institutional affiliations.

Open Access This article is licensed under a Creative Commons Attribution 4.0 International License, which permits use, sharing, adaptation, distribution and reproduction in any medium or format, as long as you give appropriate credit to the original author(s) and the source, provide a link to the Creative Commons licence, and indicate if changes were made. The images or other third party material in this article are included in the article's Creative Commons licence, unless indicated otherwise in a credit line to the material. If material is not included in the article's Creative Commons licence and your intended use is not permitted by statutory regulation or exceeds the permitted use, you will need to obtain permission directly from the copyright holder. To view a copy of this licence, visit <http://creativecommons.org/licenses/by/4.0/>.

© The Author(s) 2026

Methods

Sample locations and bulk sediment composition

For this study we used sediments from multicore PS58/270-1 and piston core PS58/270-5 recovered from a water depth of 4,981 m at 62.028° S and 116.123° W in the South Pacific (Fig. 1). The cores were recovered just south of the APF during RV *Polarstern* expedition PS58 (ANT-XVIII/5a) in 2001⁷³. We note that the section 1,995–2,095 cm was most likely curated in reverse order, so all data from this section are presented in a revised stratigraphic order.

Bulk sediment parameters were determined at the Alfred Wegener Institute Bremerhaven using standard procedures⁹, and are reported with a correction for pore-water salt content^{34,74}. Counts of clastic grains larger than 250 μm were identified from downcore X-radiographs following the method of ref. 75 and converted to $^{230}\text{Th}_{\text{xs}}$ -normalized fluxes (as described in the following). Located below the carbonate compensation depth, calcium carbonate (CaCO_3) is virtually absent in this core. The total salt-corrected carbon content is overall low at $0.19\% \pm 0.05$ (2 s.d., $n = 229$) and uncorrelated with Ca ($R^2 < 0.1$) (Extended Data Fig. 1a,b). The Ca content is thus primarily lithogenic in origin (see also the correlation with lithogenic tracer ^{232}Th shown in Extended Data Fig. 7b) and the total carbon content represents total organic carbon in PS58/270-5. The depositional environment is, however, dominated by opal¹⁶, ranging from ~30 to 90% (median of 81.4%), and terrigenous input ranging from near 0% to ~60% in PS58/270-5 (median of 18.4%) (Extended Data Fig. 1b,c).

Chronology of core PS58/270-5

The age model of core PS58/270-5 was constrained primarily by the last occurrence dates (LODs) of *Rouxia leventerae*, *Hemidiscus karstenii*, *Rouxia constricta* and *Actinocyclus ingens* and diatom-based summer sea surface temperature (SSST) reconstructions³⁴. The SSST reconstructions use the Imbrie and Kipp method adopted for diatoms with a root-mean-square error of prediction (RMSEP) of 0.83 °C (refs. 16, 76, 77). Age tie points were determined by correlation with the EDC temperature signal ($n = 19$ in total)⁶⁶ (Extended Data Fig. 2a,b). We further identified time intervals where $^{230}\text{Th}_{\text{xs}}$ -flux normalized lithogenic input tracers (such as ^{232}Th and Fe) in PS58/270-5 are similar to the dust background fluxes for core PS75/056-1 in the SAZ^{10,28,29} (Extended Data Fig. 2e). For these intervals only, the diatom-based stratigraphy was refined by tuning the high-resolution X-ray fluorescence (XRF) scanner Fe data to the EDC dust record ($n = 6$)³⁷ (Extended Data Fig. 2c,d).

The age of the youngest part of our sediment sequence at site PS58/270 was constrained by the analysis of excess ^{210}Pb ($^{210}\text{Pb}_{\text{xs}}$; analytical details are given in the following) in multicore PS58/270-1 (Extended Data Fig. 3a). Calculated $^{210}\text{Pb}_{\text{xs}}$ -derived ages yield sedimentation rates of ~89 cm ka^{-1} , which is higher than the entire older part of core PS58/270-5, with an average sedimentation rate of ~5 cm ka^{-1} for the last ~500 ka. We are unable to determine whether this high sediment accumulation is real or an artefact related for example to bioturbation or inaccuracies of the constant rate of supply model for $^{210}\text{Pb}_{\text{xs}}$ at this location. However, the fact that $^{210}\text{Pb}_{\text{xs}}$ is present in the top 5 cm of multicore PS58/270-1 provides valuable age constraints, even in the limit of changing ^{210}Pb supply and/or bioturbation. The $^{210}\text{Pb}_{\text{xs}}$ activity disappeared between depths of 4–5 cm and 10–11 cm, so we consider the mid-point at 7.5 cm as the depth where all $^{210}\text{Pb}_{\text{xs}}$ is decayed (half-life of ~22.2 a). This should be the case after eight ^{210}Pb half-lives, implying an age of ~0.18 ka BP at 7.5-cm depth. Extrapolating the resulting sedimentation rate yields an age of ~0.25 ka BP at 10.5-cm depth in PS58/270-1.

Because the top part of piston core PS58/270-5 was lost during coring, the stratigraphy was completed by splicing in multicore PS58/270-1 from the same site. Based on water content, dry bulk density and total carbon content³⁴, 1.5-cm depth in PS58/270-5 was identified to be equivalent to ~10.5-cm depth in PS58/270-1. Thus, the youngest age

tie point at 1.5 cm in PS58/270-5 is 0.17 ka BP (BP = 1950). Considering that the next tie point at 10.23 ka BP is at a depth of 92 cm (PS58/270-5 depth scale), the uncertainties in the age–depth relationship in the top few centimetres of PS58/270-1 have a negligible effect on the (Holocene section of the) age model of PS58/270-5. Including the additional tie point for the youngest part of the sediment sequence, the age model was derived from linear interpolation between the individual tie points (Extended Data Fig. 2a). Linear interpolation was chosen to avoid smoothing of the age–depth relationship across intervals of rapid change in sedimentation rate (Extended Data Figs. 4a and 5). The resulting age model is consistent with expected glacial–interglacial systematics of winter sea-ice cover reconstructed from diatom assemblages using the modern analogue technique (MAT) with a RMSEP of 5.5%^{16,34,78} (Fig. 2b).

Moreover, this age model was compared to $^{230}\text{Th}_{\text{xs}}$ -derived ages calculated following the approach described by ref. 79 (Extended Data Figs. 3b and 4b), which assumes a constant rate of supply for $^{230}\text{Th}_{\text{xs}}$ inventories over climatic cycles. The approach is typically inaccurate for the youngest part of sediment cores⁷⁹. However, our results show an overall remarkable agreement between the two independent age models for the last ~300 ka (Extended Data Fig. 4b). We analysed samples for their U-Th isotope composition only down to a depth of 1,983 cm in PS58/270-5 (corresponding to an age of ~390 ka BP), implying that the depth where $^{230}\text{Th}_{\text{xs}} = 0$ is below the depth of 1,983 cm. Therefore, the $^{230}\text{Th}_{\text{xs}}$ budget is not fully constrained by data towards the bottom of core PS58/270-5, as required for this approach⁷⁹. To calculate $^{230}\text{Th}_{\text{xs}}$ -derived ages for the deeper part, we extrapolated the exponential decrease in $^{230}\text{Th}_{\text{xs}}$ activity in the upper 1,983 cm towards the bottom of the core (Extended Data Figs. 3b and 4b). Inaccuracies in these estimates are considered to cause the systematically increased deviation of the $^{230}\text{Th}_{\text{xs}}$ -derived age model in the oldest part of the core.

^{210}Pb activity measurements

Four samples between depths of 2 and 11 cm in the multicore PS58/270-1 were analysed by non-destructive gamma spectrometry for their ^{210}Pb , ^{214}Pb and ^{214}Bi activities using an ultralow-level germanium gamma detector (Canberra GCW2522 and Canberra InSpector DeskTop) at the Institute for Chemistry and Biology for the Marine Environment (ICBM) at the University of Oldenburg³⁴. For the gamma counting, freeze-dried samples were homogenized, filled into polysulfone tubes (with a diameter of 1 cm) and compressed to a height of 3.5 cm. Before analysis, all samples were stored for one month to reach secular equilibrium between the parent isotope ^{226}Ra and its short-lived daughter products ^{222}Rn , ^{214}Pb and ^{214}Bi . Depending on the expected activity, the individual sample signals were counted for ~5–6 days. The activities of isotopes ^{210}Pb (46.4 keV), ^{214}Pb (352 keV) and ^{214}Bi (609.3 keV) were corrected for detector efficiency and intensity with certified reference material UREM-11 (uranium ore). Supported ^{210}Pb activity from the in situ decay of ^{226}Ra in the samples was determined as the activity of its short-lived daughter product ^{214}Pb . Unsupported excess ^{210}Pb ($^{210}\text{Pb}_{\text{xs}}$) activity was calculated as the difference between total ^{210}Pb activity and ^{214}Pb activity. The uncertainties ranged from ~5% for 393 Bq kg^{-1} at 2–3-cm depth to 12.5% for 198 Bq kg^{-1} at 4–5-cm depth. Estimates of age and sedimentation rates were derived from a constant rate of supply model and the logarithmic downcore decrease of $^{210}\text{Pb}_{\text{xs}}$ activity^{80,81}. These $^{210}\text{Pb}_{\text{xs}}$ -derived ages were used to constrain the youngest part of the sediment sequence at site PS58/270 as described above.

U-Th analysis of bulk sediment samples

A total of 144 samples (including five full replicate samples) were selected for U-Th analysis to calculate $^{230}\text{Th}_{\text{xs}}$ -normalized mass fluxes for the past ~400 ka. Sample preparation and analysis at Lamont-Doherty Earth Observatory (LDEO) of Columbia University followed previously published procedures^{82,83}. In brief, ~100 mg of freeze-dried bulk sediment was spiked with ^{229}Th and ^{236}U before

HClO_4 –HF– HNO_3 -based sample digestion for ion-chromatographic separation of U and Th from the sample matrix using Fe coprecipitation and 2 ml Bio-Rad AG1X-8 resin (100–200 mesh)⁸⁴. Mass spectrometric analysis of U and Th isotopes was carried out in 2% HNO_3 matrix using a Thermo Scientific Element II inductively coupled plasma mass spectrometer (ICP–MS) at LDEO. External reproducibility was estimated by repeat analysis of the VIMS reference material⁸³, yielding 3.6% for ^{230}Th , 2.8% for ^{232}Th , 3.8% for ^{234}U , 4.0% for ^{235}U and 4.0% for ^{238}U (ref. 34; 1 RSD (relative standard deviation, $n=8$). Blank contributions were below 0.1% for all analysed U and Th isotopes, except for ^{234}U , which had blank contributions of <0.3%.

The U and Th isotope data were used to calculate $^{230}\text{Th}_{\text{xs}}$ -normalized mass fluxes³⁴ following published procedures³³. This requires correction for the ^{230}Th supported by the decay of lithogenic and authigenic U, for which we used a lithogenic $^{238}\text{U}/^{232}\text{Th}$ activity ratio of 0.525 ± 0.014 (2 s.d., $n=4$) estimated internally from PS58/270-5 samples with the lowest $^{238}\text{U}/^{232}\text{Th}$ activity and the highest ^{232}Th concentrations of $8.9\text{--}10.9 \mu\text{g g}^{-1}$ (similar to the crustal average of $10.7 \mu\text{g g}^{-1}$)⁷². This lithogenic $^{238}\text{U}/^{232}\text{Th}$ activity ratio is consistent with expected values for the Southern Ocean³³. The normalized mass fluxes were calculated as

$$\text{Mass flux} = \frac{\beta_{230} \times z}{A_{230\text{Th}_{\text{xs}}}(0)}$$

where β_{230} is the production rate, z is the water depth in centimetres, and $A_{230\text{Th}_{\text{xs}}}(0)$ is the decay-corrected $^{230}\text{Th}_{\text{xs}}$ activity (ref. 33 provides details). Propagated uncertainties were calculated at the 2σ level for all $^{230}\text{Th}_{\text{xs}}$ -based element and particle flux estimates. For example, mass flux uncertainties range from -2% to -11%, with systematic increases towards the oldest part³⁴.

$^{230}\text{Th}_{\text{xs}}$ -normalized mass fluxes and traditional MARs

The accuracy of $^{230}\text{Th}_{\text{xs}}$ -normalized mass fluxes depends on the assumption that the ^{230}Th production in the overlying water column is quantitatively scavenged into the sediments. Systematic discrepancy from this basic assumption can be induced by grain size effects during sediment redistribution, CaCO_3 dissolution, hydrothermal and boundary scavenging, and the resuspension of ^{230}Th in benthic nepheloid layers³³.

The sedimentary ^{230}Th systematics were shown to be fairly robust against grain size effects resulting from sediment redistribution at the seafloor³³, in particular in the deep sea below $>1,500\text{-m}$ water depth⁸⁵. This implies that these effects are negligible at our remote core site at a water depth of 4,981 m. The location of PS58/270 in the abyssal South Pacific prohibits CaCO_3 deposition (see also the bulk sediment description above and Extended Data Fig. 1) and thus CaCO_3 -related post-depositional particle dissolution releasing scavenged ^{230}Th back to the water column. Away from active hydrothermal vents, hydrothermal scavenging can also be excluded from biasing calculated mass fluxes at site PS58/270. Our core site is located outside the region considered likely for boundary scavenging³³, but the overall relatively high particle fluxes at these latitudes may result in a surplus of ^{230}Th in PS58/270-5 sediments, implying that mass fluxes may be biased low³³. However, previous work shows no indication for systematic bias in $^{230}\text{Th}_{\text{xs}}$ -normalized fluxes at Antarctic Circumpolar Current (ACC) latitudes in the Southeast Pacific^{9,10,17,41}. The influence of benthic nepheloid layers on preserved sedimentary $^{230}\text{Th}_{\text{xs}}$ is poorly characterized³³. Yet, the extremely low bottom-layer particle concentrations in the study area⁸⁶ suggest that their influence on ^{230}Th systematics is low at site PS58/270. Moreover, any bias resulting from the processes above is expected to be reflected in a systematic offset of the $^{230}\text{Th}_{\text{xs}}$ -derived age model from the tie point-derived chronology (see also the description of core chronology already given). As this is not the case (Extended Data Fig. 4b), we consider our $^{230}\text{Th}_{\text{xs}}$ -normalized mass fluxes to be robust within the general estimated uncertainty of $\sim 30\%$ resulting from incomplete characterization of the influence of

oceanographic conditions on ^{230}Th fluxes to the sediments^{33,87}. Accordingly, our lithic baseline fluxes of $\sim 0.1 \text{ g cm}^{-2} \text{ ka}^{-1}$ are similar to previous results for the Holocene high-latitude South Pacific^{18,41}, further corroborating the robustness of the ^{230}Th -normalized flux reconstructions.

Comparing our $^{230}\text{Th}_{\text{xs}}$ -normalized mass fluxes with traditional MARs (calculated based on dry bulk densities and linear sedimentation rates) highlights the difference between the two approaches. This difference reflects variations in sediment redistribution (expressed as focusing factor Ψ in Extended Data Fig. 5) resulting from temporal changes in lateral erosion and the accumulation of sediments at site PS58/270 (Extended Data Fig. 5). It is noted that the high focusing factor around ~ 250 ka BP may result in an underestimation of $^{230}\text{Th}_{\text{xs}}$ -normalized fluxes²³ during early MIS7 (Extended Data Figs. 2e and 5). Importantly, an overall uncertainty of $\sim 30\%$ on the deep-sea ^{230}Th flux³³ appears small compared to the bias in traditional MARs at site PS58/270 (Extended Data Fig. 5).

Major and trace element analysis of bulk sediments

Major and trace element compositions of the bulk sediments were measured on a total of 144 (including five full replicates) discrete sample aliquots of $\sim 5\%$ separated from the samples digested for U–Th analysis. Samples were diluted by a factor of $\sim 2,000$ for analysis of Al, Ca, Mg, K, Fe, Ti, Ba, Sr and Y in 2% HNO_3 matrix using an Agilent 720 ICP–OES at LDEO. The element concentrations and internal 1 RSD (%) were calculated based on multiple wavelengths where available (Al, Fe, Ca, Mg, Ti, Sr, Y and Ba). Every wavelength was analysed five times during a measurement (five ‘cycles’). Where only a single wavelength was available (K, Na), the internal uncertainty represents the 1 RSD of the five cycles. External reproducibility was monitored by full procedural replicates of the VIMS reference material¹⁸³, yielding a 1 RSD better than 3.3% for all elements³⁴ ($n=8$). All samples were routinely corrected for analytical blanks, which contributed <1% for all elements included here. Full procedural blank levels were similar to the analytical blanks, so no additional blank correction was applied. Due to the high Na content in PS58/270-5 (dominated by pore-water Na: high porosity, relatively low lithogenic Na), the measured Na concentrations exceeded the calibration standards of the ICP–OES instrument and are therefore excluded.

High-resolution elemental analysis of K, Sr, Ti, Fe, Ca and Ba was performed at 1-cm downcore resolution³⁴ using an AVAATECH profiling X-ray fluorescence (XRF) core scanner at the Alfred Wegener Institute Bremerhaven following previously published procedures^{9,88}. Outliers were removed manually and the reproducibility of the XRF core scanner data was monitored routinely at the Alfred Wegner Institute using triplicate analysis of four reference materials of different composition during each analytical session. During the analytical session of PS58/270-5, signal intensities of the reference materials typically varied within 4% (calculated, per element, as $[\text{signal maximum} - \text{signal minimum}]/\text{signal average} \times 100$; average variation of 1.7%), except for Ba ($\pm 13\%$). We converted the high-resolution intensities for K, Sr, Ti, Fe, Ca and Ba measured with the XRF core scanner into quantitative concentrations using linear regressions³⁴ (Extended Data Fig. 6).

The relative weight of all sediment components was corrected for pore-water salt⁷⁴, and the reported fluxes for PS58/270-5 were normalized to $^{230}\text{Th}_{\text{xs}}$ following the procedures already described.

Tracers of export production

We used non-lithogenic barium (Ba excess: $\text{Ba}_{\text{xs}} = \text{Ba}_{\text{total}} - \text{Ba}_{\text{lithogenic}}$; where $\text{Ba}_{\text{lithogenic}} = [\text{Ba}/\text{Ti}_{\text{UCC}} \times \text{Ti}_{\text{sample}} + \text{Ba}/^{232}\text{Th}_{\text{UCC}} \times ^{232}\text{Th}_{\text{sample}}]/2$), opal and carbon fluxes as indicators of export production in the Pacific Southern Ocean^{9,34}. The positive correlation between these independent proxies ($r=0.75$ for opal and Ba_{xs} fluxes, $r=0.87$ for opal and carbon fluxes, $r=0.63$ for Ba_{xs} and carbon fluxes, all $P < 0.0001$, $n=139$) (Extended Data Fig. 7h,i) attests that they track changes in export production (and thus carbon export) at site PS58/270.

Elemental tracers of provenance and weathering

Due to the absence of calcium carbonate in PS58/270-5 (Methods section 'Sample locations and bulk sediment composition' and Extended Data Fig. 1), the concentrations of the alkali and alkaline earth elements K, Ca, Mg and Sr are controlled by changes in lithic input (Extended Data Fig. 7a,b,d,f). These elements are more susceptible to partial dissolution during chemical weathering of silicate minerals^{44,8990}, so their correlation with the rather insoluble (refractory) elements (Al, Ti and ^{232}Th) is overall lower, except for K (Extended Data Fig. 7a,b,d,f). Accordingly, the relative abundance of refractory to more mobile elements provides information on the mineralogy/chemical maturity of the lithogenic particle input in core PS58/270-5. In other words, highly weathered material is depleted in more soluble elements relative to refractory elements and is expected to have an overall lower partial solubility. This can be expressed as elemental ratios such as Ti/Ca, or indices such as the CIA, calculated as $\text{CIA} = \text{Al}_2\text{O}_3 / (\text{Al}_2\text{O}_3 + \text{CaO}^* + \text{Na}_2\text{O}^* + \text{K}_2\text{O}) \times 100$, using molar proportions⁴⁴ (CaO^* and Na_2O^* refer to the CaO and Na_2O of the lithogenic fraction). Due to the high content of pore-water Na in our samples, Na_2O^* was derived from CaO* in PS58/270-5 and an upper continental crust Na/Ca of 0.963 (ref. 72).

Statistical analysis

The statistical analyses reported in the main text and in Extended Data Figs. 6–8 are based on Pearson's correlation coefficient and two-sided *P* values using *n* = 139 samples and *n* – 2 degrees of freedom, if not stated otherwise.

Data availability

All data presented in this paper are included in this published Article and in the PANGAEA database at <https://doi.org/10.1594/PANGAEA.982690>.

References

73. Miller, H. Expeditionsprogramm Nr. 59, FS Polarstern, ANT-XVIII/5a (Alfred-Wegener-Institute for Polar- and Marine Research, 2001); <https://epic.awi.de/id/eprint/29833/>
74. Kuhn, G. Don't forget the salty soup: calculations for bulk marine geochemistry and radionuclide geochronology. *Mineral. Mag.* **77**, 1519 (2013).
75. Grobe, H. A simple method for the determination of ice-rafted debris in sediment cores. *Polarforschung* **57**, 123–126 (1987).
76. Esper, O. & Gersonde, R. Quaternary surface water temperature estimations: new diatom transfer functions for the Southern Ocean. *Palaeogeogr. Palaeoclimatol. Palaeoecol.* **414**, 1–19 (2014).
77. Esper, O., Benz, V. & Gersonde, R. Diatoms abundance in sediment core PS58/270-5. PANGAEA <https://doi.org/10.1594/PANGAEA.860926> (2016).
78. Esper, O. & Gersonde, R. New tools for the reconstruction of Pleistocene Antarctic sea ice. *Palaeogeogr. Palaeoclimatol. Palaeoecol.* **399**, 260–283 (2014).
79. Geibert, W., Stimac, I., Rutgers van der Loeff, M. M. & Kuhn, G. Dating deep-sea sediments with ^{230}Th excess using a constant rate of supply model. *Paleoceanogr. Paleoclimatol.* **34**, 1895–1912 (2019).
80. Chuang, P.-C. et al. Nutrient turnover by large sulfur bacteria on the Namibian mud belt during the low productivity season. *Front. Mar. Sci.* <https://doi.org/10.3389/fmars.2022.929913> (2022).
81. Huh, C.-A., Lin, H.-L., Lin, S. & Huang, Y.-W. Modern accumulation rates and a budget of sediment off the Gaoping (Kaoping) River, SW Taiwan: a tidal and flood dominated depositional environment around a submarine canyon. *J. Mar. Syst.* **76**, 405–416 (2009).
82. Costa, K. M. et al. Trace element (Mn, Zn, Ni, V) and authigenic uranium (aU) geochemistry reveal sedimentary redox history on the Juan de Fuca Ridge, North Pacific Ocean. *Geochim. Cosmochim. Acta* **236**, 79–98 (2018).
83. Costa, K. & McManus, J. Efficacy of ^{230}Th normalization in sediments from the Juan de Fuca Ridge, Northeast Pacific Ocean. *Geochim. Cosmochim. Acta* **197**, 215–225 (2017).
84. Fleisher, M. Q. & Anderson, R. F. Assessing the collection efficiency of Ross Sea sediment traps using ^{230}Th and ^{231}Pa . US South. Ocean JGOFS Program AESOPS Part III **50**, 693–712 (2003).
85. Tomchovska, I. et al. Fractionation during sediment winnowing drives divergent mass accumulation rates derived from ^{230}Th and ^3He on the Cocos Ridge. *Geochim. Cosmochim. Acta* **395**, 149–165 (2025).
86. Gardner, W. D., Jo Richardson, M., Mishonov, A. V. & Biscaye, P. E. Global comparison of benthic nepheloid layers based on 52 years of nephelometer and transmissometer measurements. *Prog. Oceanogr.* **168**, 100–111 (2018).
87. Henderson, G. M., Heinze, C., Anderson, R. F. & Winguth, A. M. E. Global distribution of the ^{230}Th flux to ocean sediments constrained by GCM modelling. *Deep Sea Res. Part Oceanogr. Res. Pap.* **46**, 1861–1893 (1999).
88. Jacobi, L., Nürnberg, D., Chao, W., Lembke-Jene, L. & Tiedemann, R. ENSO vs glacial-interglacial-induced changes in the Kuroshio-Oyashio transition zone during the Pleistocene. *Front. Mar. Sci.* <https://doi.org/10.3389/fmars.2023.1074431> (2023).
89. Douglas, G. B., Gray, C. M., Hart, B. T. & Beckett, R. A strontium isotopic investigation of the origin of suspended particulate matter (SPM) in the Murray-Darling River system, Australia. *Geochim. Cosmochim. Acta* **59**, 3799–3815 (1995).
90. Kamber, B. S., Greig, A. & Collerson, K. D. A new estimate for the composition of weathered young upper continental crust from alluvial sediments, Queensland, Australia. *Geochim. Cosmochim. Acta* **69**, 1041–1058 (2005).
91. Condie, K. C. Chemical composition and evolution of the upper continental crust: contrasting results from surface samples and shales. *Chem. Geol.* **104**, 1–37 (1993).
92. Simpson, G. & Aslund, T. Diorite and gabbro of the Dromedary mafic complex, South Victoria Land, Antarctica. *N. Z. J. Geol. Geophys.* **39**, 403–414 (1996).

Acknowledgements

We acknowledge the captain, crew and science team of RV *Polarstern* cruise PS58 for collecting sample material. We thank R. Schwartz for support during sample preparation and ICP–OES analysis, and M. Fleisher for help with U–Th sample analysis during the peak of the pandemic. K. Pahnke is thanked for discussion and comments on an earlier version of the manuscript. We acknowledge financial support from the Ministry of Science and Culture of the State of Lower Saxony (MWK), the DFG through grant STR 1618/1-1 (#412785502) to T.S. and the Helmholtz Association.

Author contributions

T.S., F.L. and G.W. designed the research. T.S. carried out the geochemical analyses and led the drafting of this manuscript. F.G. contributed the ^{210}Pb data. F.L. and G.W. provided sample material and laboratory infrastructure. J.P.K., O.E., G.K. and L.L.-J. contributed IRD, diatom assemblage, bulk sediment property and XRF scanner data, respectively. All authors contributed to data interpretation and revision of the manuscript.

Funding

Open access funding provided by Carl von Ossietzky Universität Oldenburg.

Competing interests

The authors declare no competing interests.

Additional information

Extended data is available for this paper at <https://doi.org/10.1038/s41561-025-01911-0>.

Supplementary information The online version contains supplementary material available at <https://doi.org/10.1038/s41561-025-01911-0>.

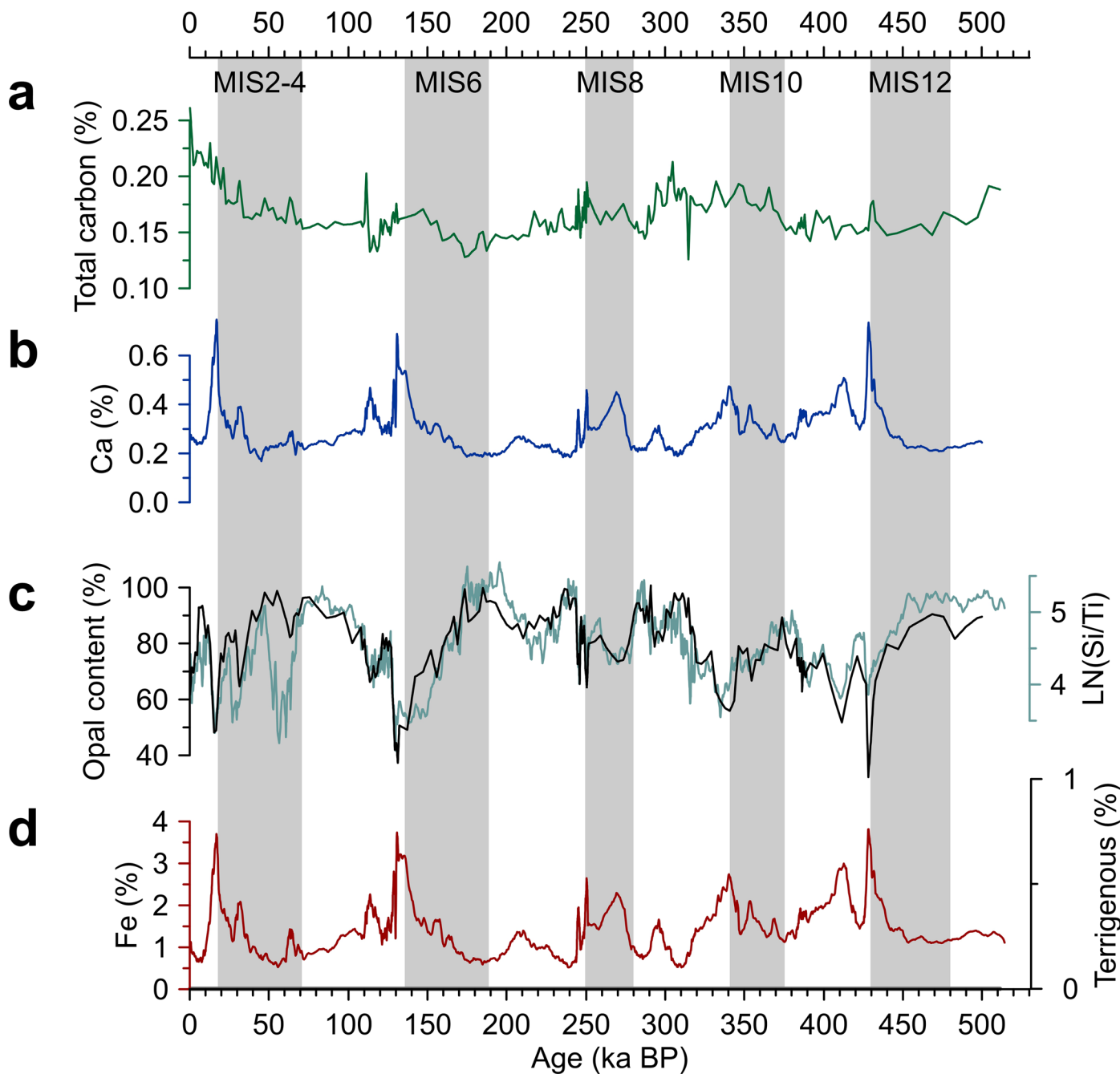
Correspondence and requests for materials should be addressed to Torben Struve.

Peer review information *Nature Geoscience* thanks Marion

Fourquez and the other, anonymous, reviewer(s) for their contribution to the peer review of this work. Primary Handling Editor: Camilla Brunello and Aliénor Lavergne, in collaboration with the *Nature Geoscience* team.

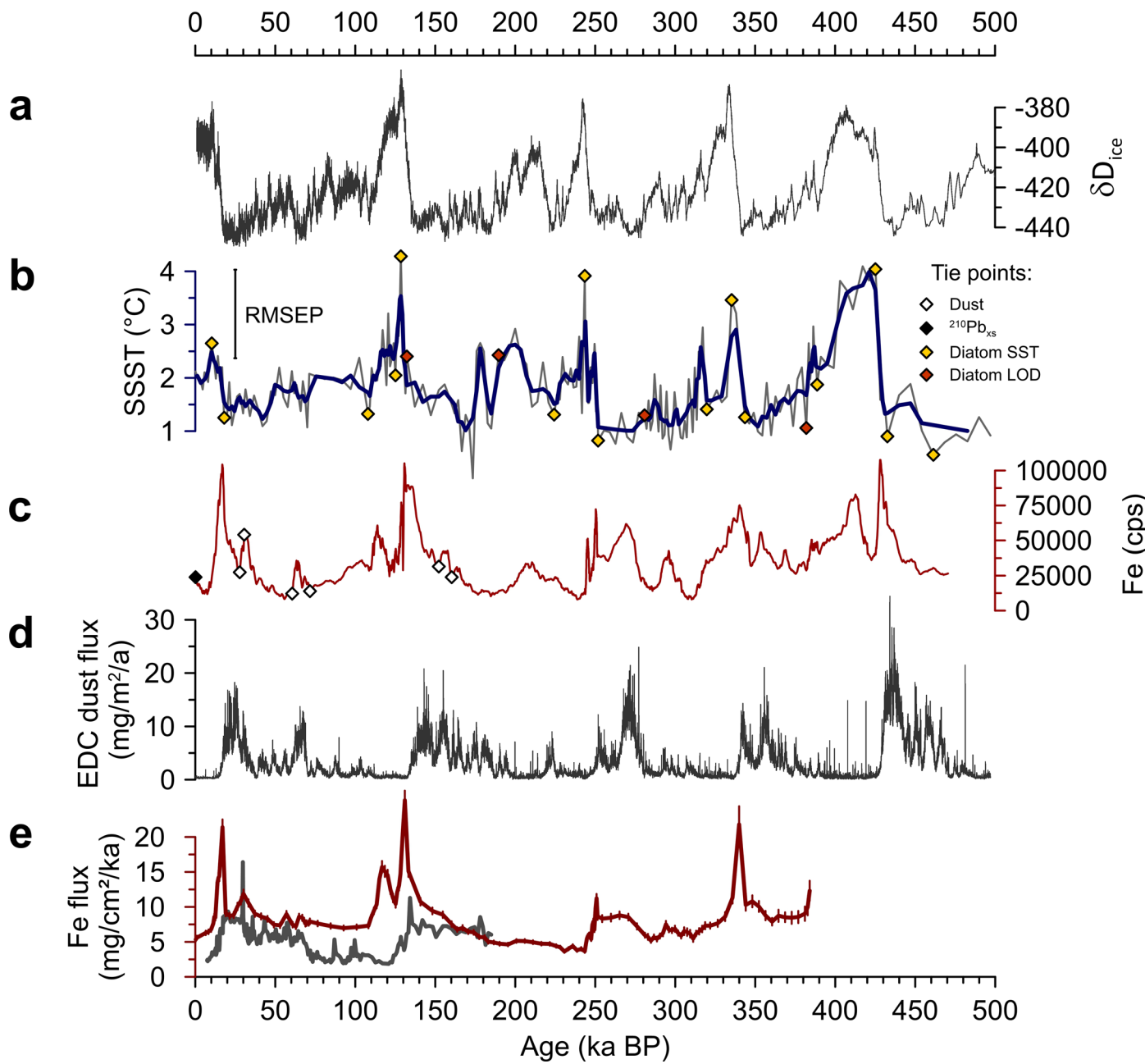
Reprints and permissions information is available at

www.nature.com/reprints.



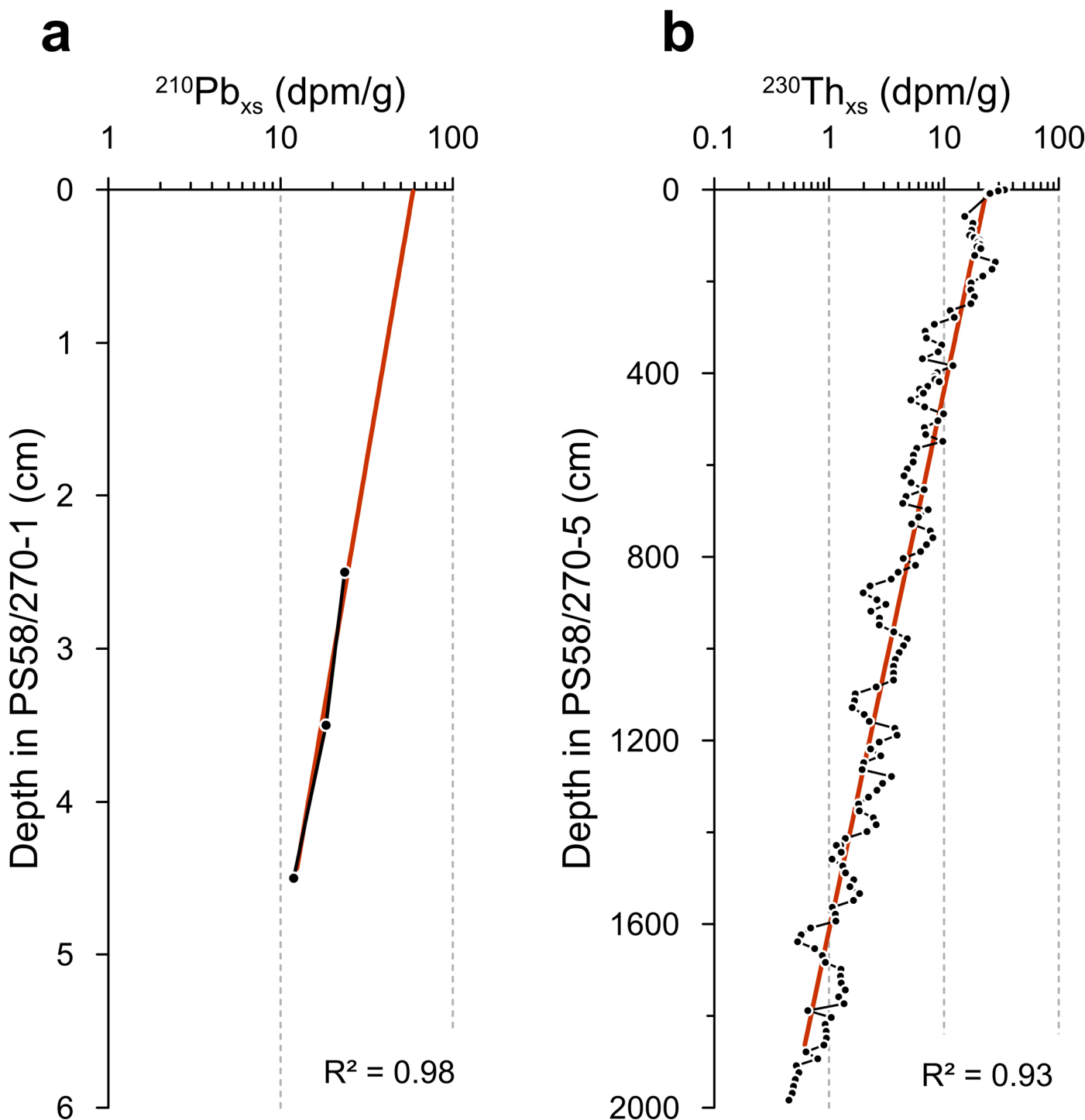
Extended Data Fig. 1 | Indicators for bulk sediment composition of PS58/270-5. (a) Total carbon content. (b) Calibrated calcium (Ca) concentrations (see also Extended Data Fig. 6e). (c) Opal content and the natural logarithm (LN) of XRF scanner silicon/titanium (Si/Ti). (d) Calibrated iron (Fe) concentrations

in red (see also Extended Data Fig. 6d) and terrigenous content calculated by subtraction of total carbon (%) and opal (%) from 100 %. MIS = Marine Isotope Stage. See Methods for more details.

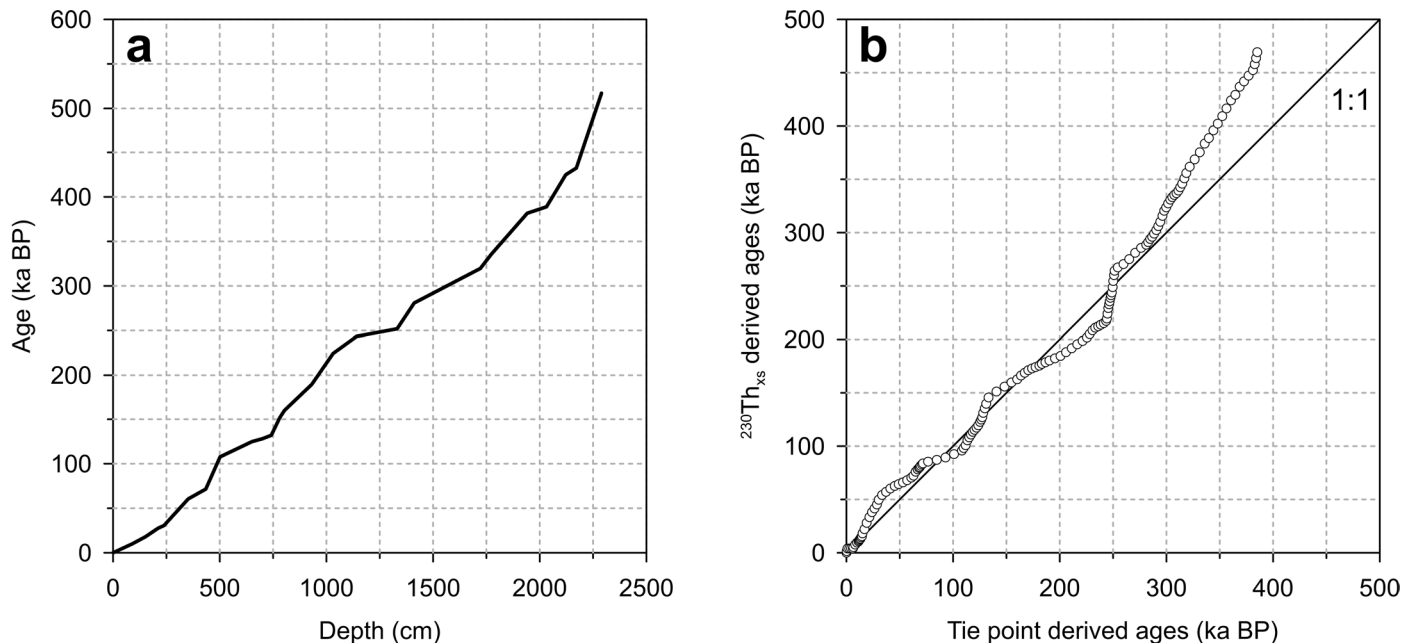


Extended Data Fig. 2 | Datasets used for defining stratigraphic tie points in core PS58/270-5. (a) EPICA Dome C ice core deuterium isotope (δD) data⁶⁶. (b) Summer sea surface temperature (SSST) reconstruction (grey) and five point running average (blue) for core PS58/270-5^{16,34,76}. RMSEP = root mean square error of the temperature prediction^{34,76}. (c) Iron (Fe) XRF scanner data for core

PS58/270-5 (five point running average). (d) Dust flux reconstruction from EPICA Dome C³⁶. (e) Iron (Fe) flux reconstruction for core PS58/270-5 (red) (error bars indicate propagated uncertainty) and subantarctic core PS75/056-1 (grey)¹⁰. Tie points are indicated by diamonds in panels (b) and (c). LOD: last occurrence date.

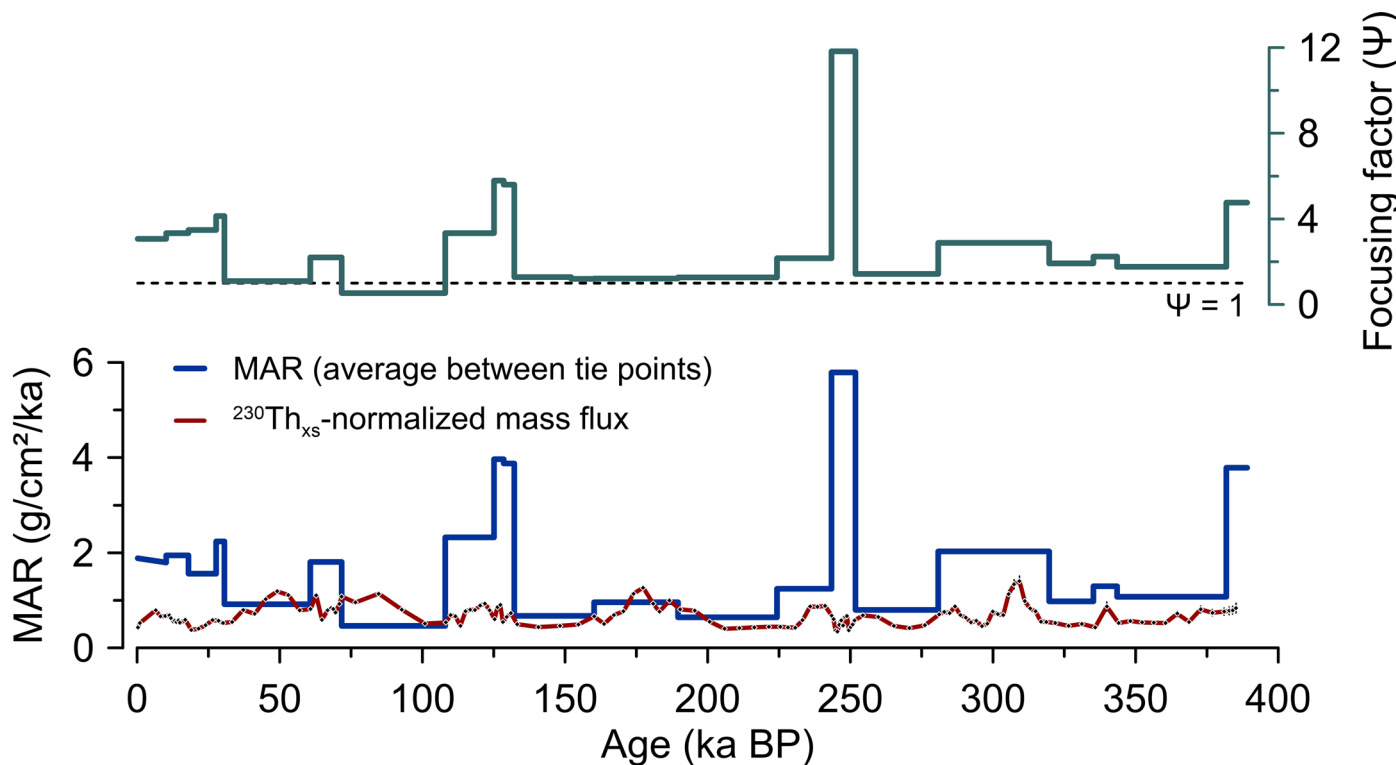


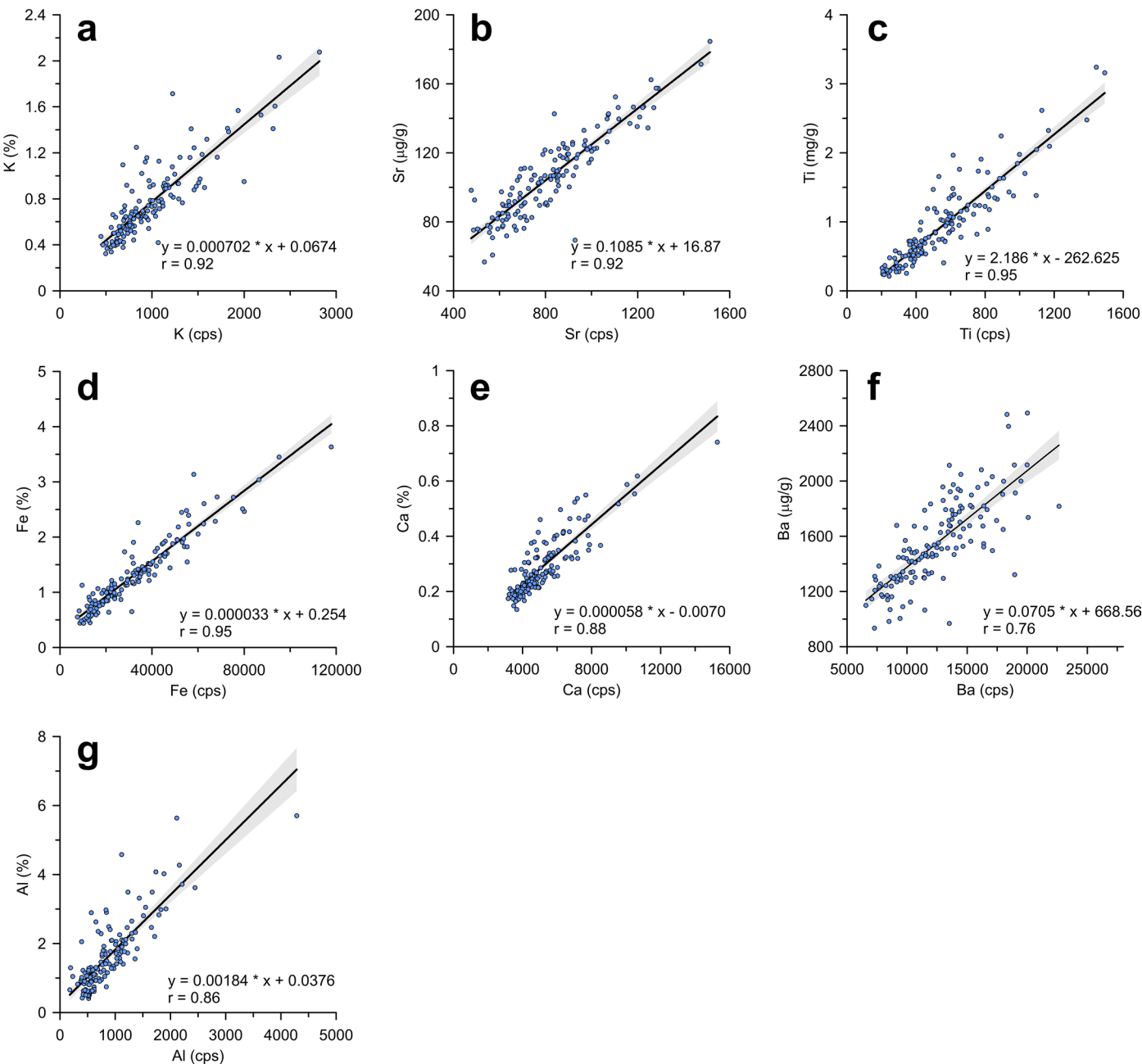
Extended Data Fig. 3 | Radioactive isotope data for PS58/270-1 and PS58/270-5. (a) Measured (black circles) excess ^{210}Pb ($^{210}\text{Pb}_{\text{xs}}$) for core PS58/270-1 and (b) for $^{230}\text{Th}_{\text{xs}}$ in PS58/270-5. The log fit in both panels (red) demonstrates the dominating effect of decay on the downcore abundance of $^{210}\text{Pb}_{\text{xs}}$ and $^{230}\text{Th}_{\text{xs}}$, highlighting the use of $^{230}\text{Th}_{\text{xs}}$ as a dating tool as described by ref. 79.



Extended Data Fig. 4 | Age model results for core PS58/270-5. (a) Age-depth plot based on tie points (Extended Data Fig. 2). (b) Comparison of manual tuning of tie points (see Extended Data Fig. 2) with $^{230}\text{Th}_{\text{xs}}$ -derived age constraints for

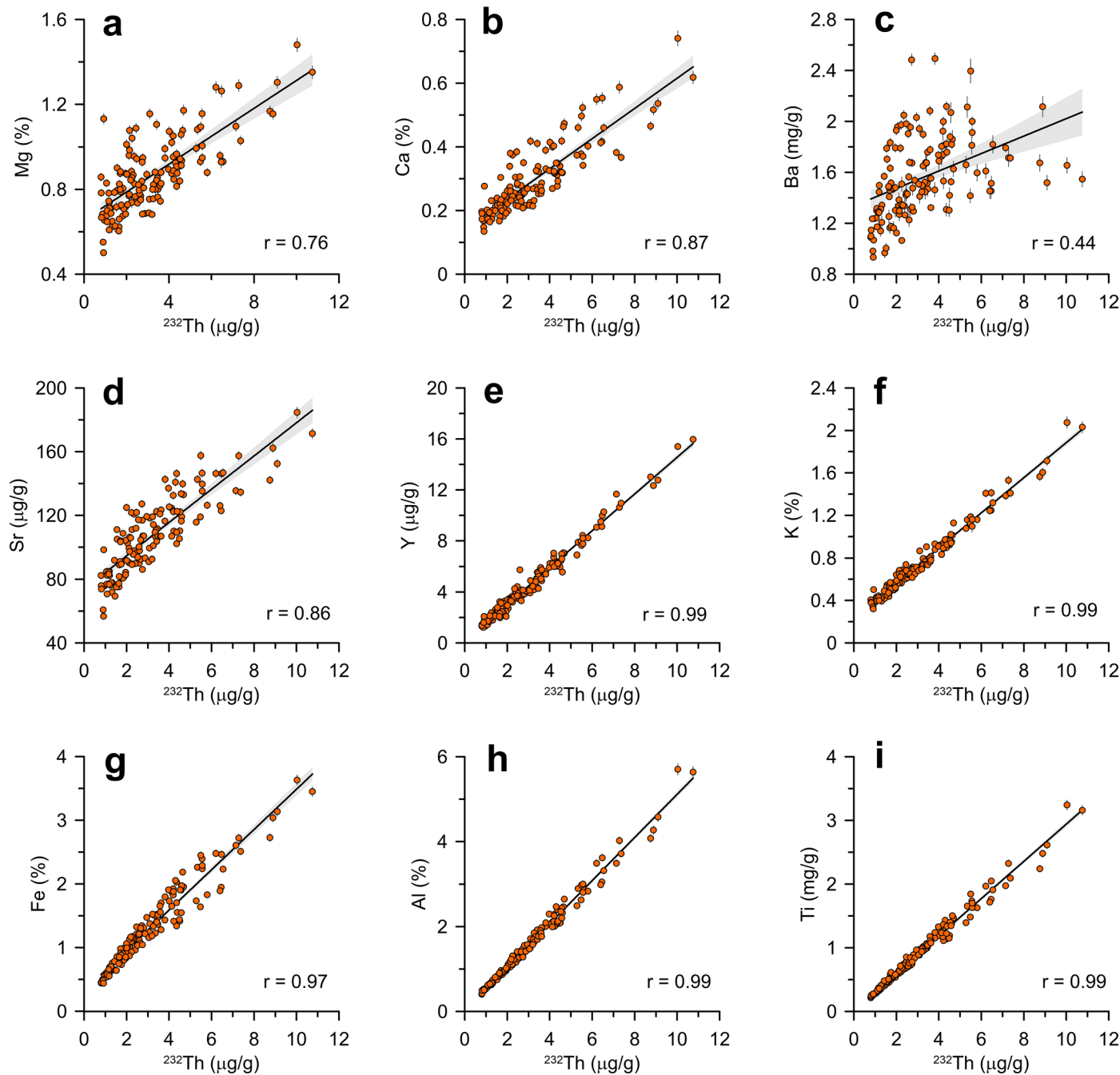
core PS58/270-5 (white dots) after ref. 79. Black line: 1:1 relationship between the two age models (perfect agreement). Note that the part older than ~300 ka BP is not very well-constrained for its $^{230}\text{Th}_{\text{xs}}$ content (see Methods for more details).





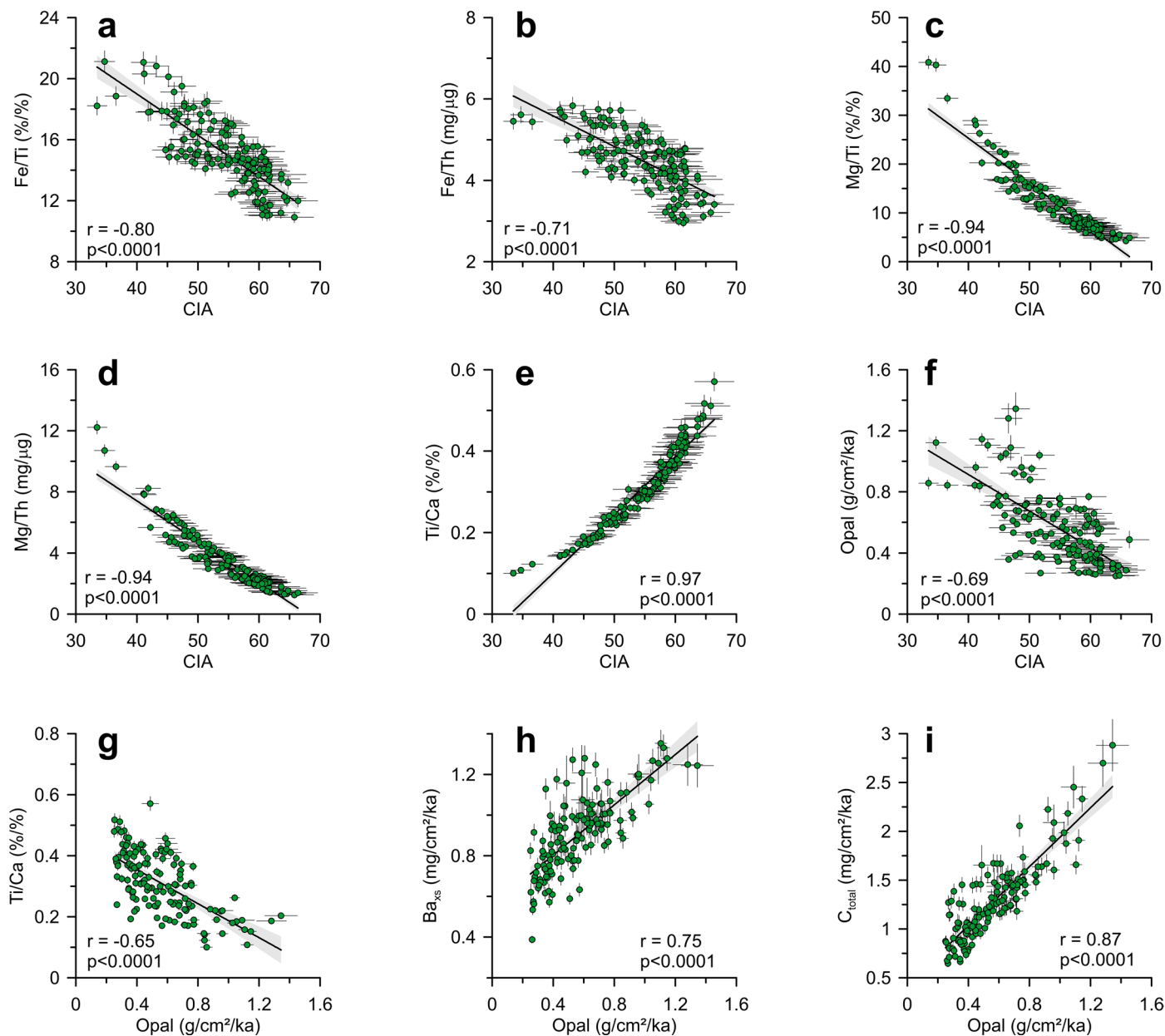
Extended Data Fig. 6 | Calibration of XRF scanner data with discrete sample results measured with ICP-OES. (a) Potassium (K). (b) Strontium (Sr). (c) Titanium (Ti). (d) Iron (Fe). (e) Calcium (Ca). (f) Barium (Ba). (g) Aluminium (Al). All XRF scanner data in (a) – (g) are the peak area signal intensities. Linear

regressions calculated for $n = 137$ samples (no XRF scanner data at the depth of $n = 2$ discrete samples, except for (a) and (c) where $n = 139$ samples) used to calibrate high resolution XRF-scanner data. Grey shadings indicate 95% confidence intervals. See Methods for more details.



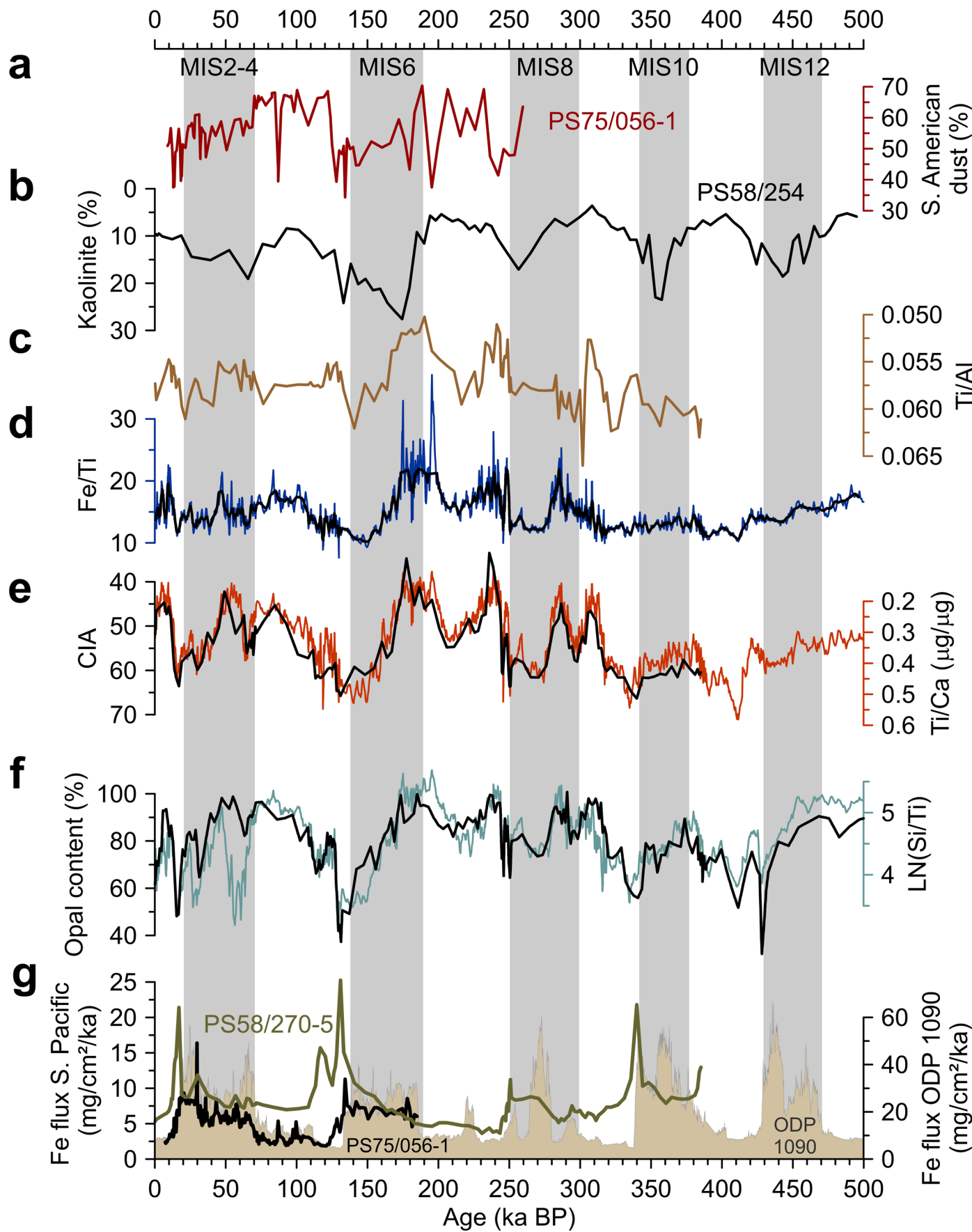
Extended Data Fig. 7 | Cross plots of elemental concentration data for core PS58/270-5. Note the strong correlation between the lithogenic tracers yttrium (Y), potassium (K), iron (Fe), aluminum (Al) and titanium (Ti) with ^{232}Th and the reduced correlation of ^{232}Th with magnesium (Mg), calcium

(Ca), barium (Ba) and strontium (Sr) in panels (e) – (i) and (a) – (d), respectively. Linear regressions, Pearson's r and two-tailed p -values (all <0.0001) calculated for $n = 139$ samples. Grey shadings indicate 95% confidence intervals. See also Methods for more details.



Extended Data Fig. 8 | Cross plots of indicators of sediment mineralogy and export production for core PS58/270-5. (a) Ratio of iron (Fe) and titanium (Ti) vs. CIA (Chemical Index of Alteration = $\text{Al}_2\text{O}_3/[\text{Al}_2\text{O}_3 + \text{CaO}^* + \text{Na}_2\text{O}^* + \text{K}_2\text{O}] \times 100$)⁴⁴. (b) Ratio of Fe and thorium (Th) vs. CIA. (c) Ratio of Mg and Ti vs. CIA. (d) Ratio of Mg and Th vs. CIA. (e) Ratio of Ti and calcium (Ca) vs. CIA. (f) Opal flux vs. CIA. (g) Ti/Ca vs. opal flux. (h) Non-lithogenic barium excess (Ba_{xs}) flux vs. opal flux. (i) Total carbon (C_{total}) vs. opal fluxes. Note that

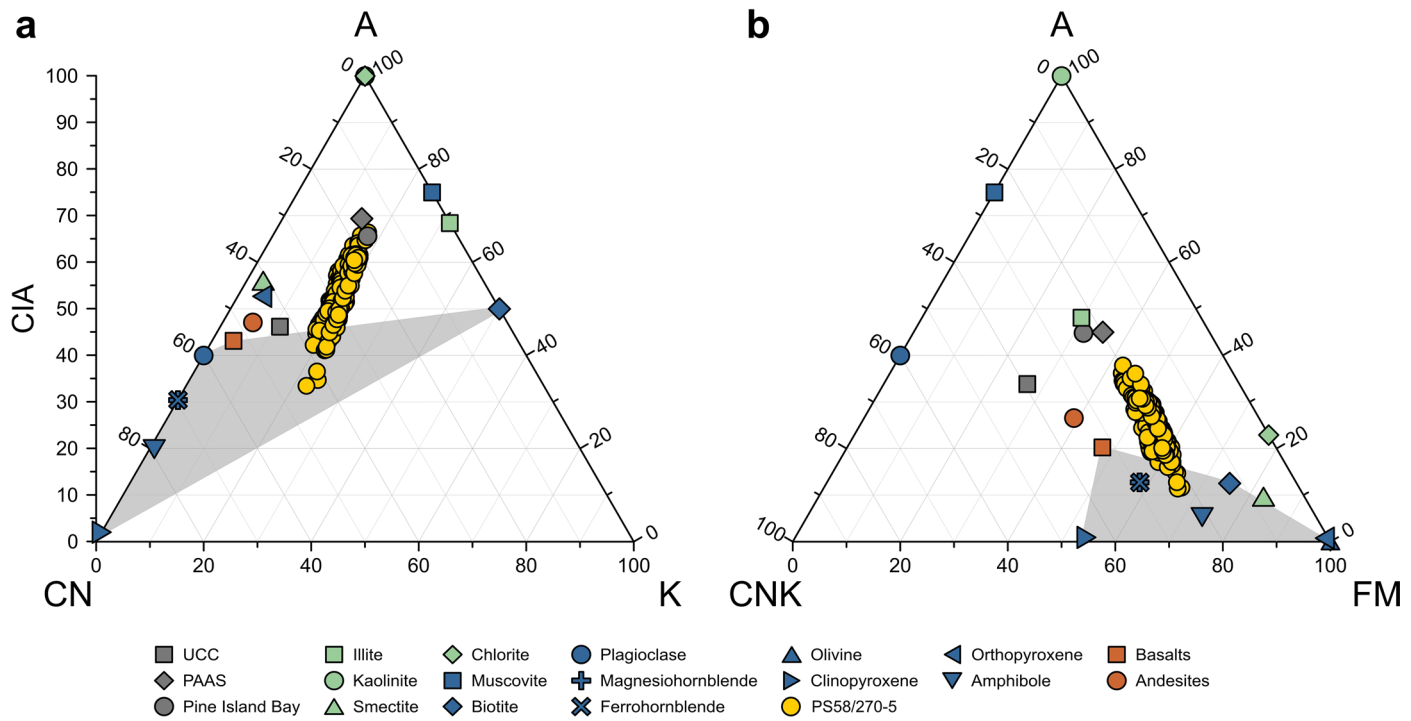
Ba_{xs} flux shows a similar relationship with CIA as opal fluxes in (f), albeit with lower r of -0.38 ($p < 0.0001$), while r for CIA and C_{total} fluxes is -0.52 . Linear regressions, Pearson's r and two-tailed p -values calculated for $n = 139$ samples. Grey shadings indicate 95% confidence intervals. Non-linear regressions yield slightly better regression coefficients for (c) – (e). Error bars indicate propagated errors. See Methods for more details.



Extended Data Fig. 9 | See next page for caption.

Extended Data Fig. 9 | Sediment composition of core PS58/270-5 in comparison with Southern Ocean lithogenic input tracers. (a) Fraction of South American dust delivered to site PS75/056 in the subantarctic South Pacific. (b) Kaolinite content in the clay fraction of site PS58/254 as an indicator of old weathered sediment input in the Amundsen Sea³² (Fig. 1). (c) Ratio of titanium (Ti) and aluminum (Al) and (d) iron (Fe) and Ti in bulk sediments of core PS58/270-5. (e) Chemical Index of Alteration (CIA) in bulk sediments of core PS58/270-5

calculated using molar proportions as $CIA = Al_2O_3/[Al_2O_3 + CaO^* + Na_2O^* + K_2O] \times 100^{44}$ (see Methods for more details) superimposed on the Ti to calcium (Ca) ratio. (f) Opal content from leaching compared with the natural logarithm (LN) of silicon (Si) to Ti ratios from XRF scanning of core PS58/270-5. (g) Comparison of dust-Fe fluxes for subantarctic core PS75/056-1¹⁰, South Pacific Antarctic Zone core PS58/270-5 and ODP Site 1090 in the subantarctic South Atlantic².



Extended Data Fig. 10 | Ternary diagrams of major element composition for PS58/270-5. (a) A-CN-K diagram ($A = Al_2O_3$, $CN = CaO^* + Na_2O^*$, $K = K_2O$) and Chemical Index of Alteration (CIA) after ref. 44. Upper Continental Crust (UCC), Post-Archaean Australian Shale (PAAS), Basalts, Andesites^{72,90,91}, Pine Island Bay sediments⁵⁰ and selected rock mineral compositions⁹² representing

possible endmembers for PS58/270-5 samples (yellow dots). (b) A-CN-K-FM diagram ($A = Al_2O_3$, $CNK = CaO^* + Na_2O^* + K_2O$, $FM = FeO + MgO$). Symbols as in (a) (see Methods for further details). All data in panels (a) and (b) are presented in molar proportions⁴³. Grey areas indicate Fe-rich rock and rock mineral compositions with low CIA.